Were chondrites magnetized by the early solar wind?

Rona Oran [a,*], Benjamin P. Weiss [a], Ofer Cohen [b]

[a] *Department of Earth, Atmospheric, and Planetary Sciences, Massachusetts Institute of Technology, 77 Massachusetts Avenue, Cambridge, MA 02139, USA*
[b] *Lowell Center for Space Science and Technology, University of Massachusetts, Lowell, MA 01854, USA*

A B S T R A C T

Chondritic meteorites have been traditionally thought to be samples of undifferentiated bodies that never experienced large-scale melting. This view has been challenged by the existence of post-accretional, unidirectional natural remanent magnetization (NRM) in CV carbonaceous chondrites. The relatively young inferred NRM age [∼10 million years (My) after solar system formation] and long duration of NRM acquisition (1–10^6 y) have been interpreted as evidence that the magnetizing field was that of a core dynamo within the CV parent body. This would imply that CV chondrites represent the primitive crust of a partially differentiated body. However, an alternative hypothesis is that the NRM was imparted by the early solar wind. Here we demonstrate that the solar wind scenario is unlikely due to three main factors: 1) the magnitude of the early solar wind magnetic field is estimated to be <0.1 µT in the terrestrial planet-forming region, 2) the resistivity of chondritic bodies limits field amplification due to pile-up of the solar wind to less than a factor of 3.5 times that of the instantaneous solar wind field, and 3) the solar wind field likely changed over timescales orders of magnitude shorter than the timescale of NRM acquisition. Using analytical arguments, numerical simulations and astronomical observations of the present-day solar wind and magnetic fields of young stars, we show that the maximum mean field the ancient solar wind could have imparted on an undifferentiated CV parent body is <3.5 nT, which is 3–4 and 3 orders of magnitude weaker than the paleointensities recorded by the CV chondrites Allende and Kaba, respectively. Therefore, the solar wind is highly unlikely to be the source of the NRM in CV chondrites. Nevertheless, future high sensitivity paleomagnetic studies of rapidly-cooled meteorites with high magnetic recording fidelity could potentially trace the evolution of the solar wind field in time.

© 2018 Elsevier B.V. All rights reserved.

1. Introduction

The accretional textures of chondritic meteorites indicate they did not undergo planetary melting processes. This has been traditionally interpreted to mean that their parent bodies did not experience endogenic melting in their interiors, and that large-scale differentiation and core formation did not take place (Weiss and Elkins-Tanton, 2013). Nevertheless, it has long been recognized that the Allende meteorite, a CV carbonaceous chondrite, contains intense NRM that is unidirectional across scales of at least ∼10 cm and is a record of an ancient field of ∼30–100 µT. This observation, reproduced by five separate laboratories over nearly five decades (see references in Carporzen et al., 2011, plus a subsequent study by Muxworthy et al., 2017), indicates that the CV parent body was cooled or aqueously altered in an ancient magnetic field after accretion.

Initially, the magnetizing field was assumed to be the field of the solar nebula (Nagata, 1979). However, the inferred formation age of Allende's magnetization apparently postdates the lifetime of the solar nebula: the NRM was dated by I-Xe thermochronometry to 9–11 My after the formation of calcium aluminum-rich inclusions (CAIs), while the nebula dispersed by ∼4 My after CAI formation (Wang et al., 2017; Weiss et al., 2017), indicating that the magnetizing field was unlikely to be nebular in origin (here we take the time of solar system formation just after the collapse of the parent molecular cloud to be the time of CAI formation at 4567.3 ± 0.16 My ago; Connelly et al., 2012). Unidirectional NRM formed after ∼4 My has also been identified in the CV chondrites ALH 84028 and ALH 85006 (Klein et al., 2014) and post-accretional NRM has also been observed in the CV chondrite Kaba (Gattacceca et al., 2016). Muxworthy et al. (2017) proposed that Allende recorded a uniform thermoremanent magnetization nearly instantaneously due to heating by impacts (although see Scheinberg et al., 2015, for an alternative view). They interpreted the NRM to be a record of a ∼6 µT paleofield whose source is either a transient impact-generated field or a nebular field dated prior to ∼4 My after CAI formation.

These results have motivated the proposal that the magnetizing field was that of a core dynamo which, unlike the solar nebular field, could have persisted for hundreds of My (Carporzen et al., 2011; Elkins-Tanton et al., 2011; Weiss and Elkins-Tanton, 2013). This picture was recently supported by Shah et al. (2017), who suggested that the CV chondrite Vigarano recorded a uniform field post-accretionally, with a mean strength of ∼4 µT. They proposed that the magnetization could be shock remanent magnetization acquired in the presence of a core dynamo. A core dynamo field implies that the CV parent body was partially differentiated and had a metallic core overlain by a melted silicate mantle and relic chondritic crust. Such a view is at odds with the traditional view that chondrite parent bodies did not experience large-scale melting and were undifferentiated. Nevertheless, unidirectional, postaccretional magnetization has subsequently been identified in CM carbonaceous chondrites (Cournède et al., 2015) and H chondrites (Bryson et al., 2016) (Table S1), hinting at the possibility that partially differentiated chondrite parent bodies may have been common in the early solar system.

1.1. The hypothesis of asteroid magnetization by the solar wind

The core dynamo proposal for chondrite paleomagnetism has been recently challenged by an alternative hypothesis: that chondrites were magnetized by the solar wind (Tarduno et al., 2017). This proposal is surprising because the solar wind today certainly could not produce chondrite magnetization due to the fact that its present-day magnetic field is typically 2–7 nT at Earth's orbit, which is 3 to 4 orders of magnitude lower than the paleointensities for CV chondrites (Table S1). To achieve the required field intensity, two effects were proposed. First, it was suggested that the early solar wind magnetic field was likely more intense than that of today. Second, it was suggested that when the wind encounters the chondrite body, it piles up against it to form a region of amplified field. Tarduno et al. (2017) hypothesized that this amplified field would explain CV paleomagnetism.

1.2. Challenges associated with the solar wind magnetization hypothesis

There are three major difficulties that the solar wind magnetization hypothesis must overcome. First, the solar wind field at ∼10 My after solar system formation is not well known. There are no direct measurements of the early solar wind, and winds of Sun-like young stellar objects (YSOs) are difficult to detect spectroscopically due to their low emission (Wood et al., 2015).

Second, amplification of the solar wind field by the body would occur only if the body causes the wind to slow down and pile up against it. Pile-up regions have been found around two kinds of planetary bodies: magnetized planets, such as Earth, Mercury, Jupiter, and Saturn (whose magnetospheres can deflect the wind) and non-magnetized bodies that have ionospheres, such as Venus and comets (which can exert a gas pressure on the wind and support an induced magnetosphere) (Kivelson and Russell, 1995). In contrast, non-magnetized and airless bodies with largely nonconductive, silicate interiors lack either mechanism for slowing down the wind (e.g., the Moon; Kivelson and Russell, 1995). Given that the solar wind hypothesis for CV chondrite paleomagnetism considers a small, airless, undifferentiated body, a pileup could only occur for an exceptionally high wind speed and exceptionally high electrical conductivity of the body's interior (Section 4).

A third factor is the temporal variability of the wind. The bulk paleointensities of most chondrites (Table S1) are a record of the vector mean field magnitude recorded over periods ranging from years to millions of years (Section 2). On the other hand, the solar wind varies on a wide range of timescales. Apart from turbulent variations, the magnetic field exhibits large-scale semi-periodic reversals in direction over timescales of days to years (Section 7). It is crucial to consider the mean field experienced by an orbiting planetary object and not just the instantaneous values.

1.3. Goals

We test the solar wind magnetization hypothesis in four stages:

I. We estimate the properties of the Sun and its surface magnetic field at the time Allende's NRM was acquired (∼10 My after solar system formation) using observations of solar analogs and constraints from the meteoritic record (Sections 2 and 3).
II. We adopt a coronal model of a young solar-like star (Cohen et al., 2010) as a proxy for the Sun at 10 My and derive a range of solar wind conditions at 2.5 AU from the Sun that could have existed at that time (Section 3).
III. The predicted solar wind properties are used as input to a suite of magnetohydrodynamic (MHD) simulations of the interaction of the wind with a hypothetical undifferentiated chondrite parent body including magnetic field diffusion inside the body. We identify the most favorable case for field amplification by the body. In the Supplementary Material, we show that the MHD approximation is appropriate in this regime due to the large magnetic field of the ancient solar wind. To our knowledge, these are the first simulations of the interaction of the wind with a non-magnetized, airless body having a chondritic resistivity, and thus of an interaction dominated by magnetic diffusion in the interior of the body (Section 6).
IV. We perform a statistical analysis of solar wind variability to estimate the mean field induced on the body over the timescales of magnetization (Section 7).

This paper is organized as follows. In Section 2, we summarize the paleomagnetic observations to be explained. In Section 3, we estimate the solar wind field strength at 10 My after solar system formation. In Section 4, we present an analytic description of the role of resistivity in solar wind pileup. In Section 5, we describe the numerical model of the wind flow around the parent body. In Sections 6 and 7, we present the results of the simulations and discuss the role of solar wind variability. In Section 8, we present our conclusions, showing that moderate field amplification at the body and the variability of the solar wind imply that undifferentiated chondritic bodies cannot have been significantly magnetized by the solar wind and that other magnetic field sources are more plausible.

2. Timeline of meteorite magnetization

A key constraint for identifying the origin of the field that magnetized chondrites is the timing of NRM acquisition (Fig. 1 and Tables S1 and S2). The first large-scale magnetic field in the solar system was likely that of the ionized nebula, which was in turn probably inherited from the parent molecular cloud (Desch and Mouschovias, 2001). Records of a 5–∼50 µT nebular field in our solar system at 1–3 My after CAI formation have been identified using paleomagnetic measurements of chondrules from the LL chondrite Semarkona (Fu et al., 2014). Disk magnetic fields may also have been observed in other systems of similar age (Stephens et al., 2014), although the interpretation of the observations as an evidence of a magnetic field are not conclusive (Kataoka et al., 2015).

Furthermore, recent paleomagnetic analyses of volcanic angrites (Wang et al., 2017) and the ungrouped achondrite NWA 7325 (Weiss et al., 2017) show that the magnetic field was indistinguishable from zero (<0.6 µT and <1.7 µT, respectively) by 3.8 and 4.2 My after CAI formation, respectively. As discussed in
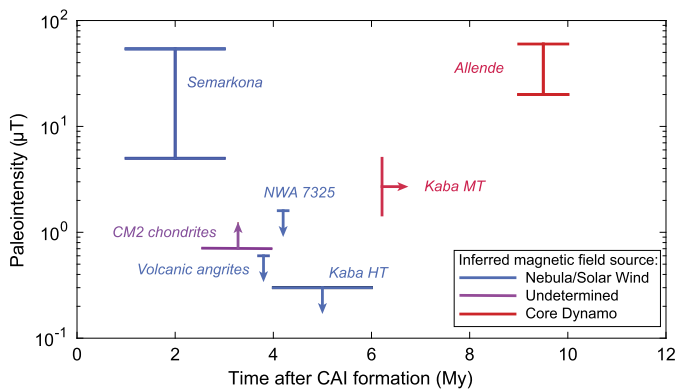
Fig. 1. Compilation of paleomagnetic observations from meteorites from the early solar system, showing the paleointensity as a function of time after CAI formation. The data are listed in Tables S1 and S2. Blue data mark constraints on the nebular and solar wind field (Table S2), red data have been interpreted to reflect parent body magnetic fields, and purple data may reflect either solar wind or parent-body fields. The Semarkona paleointensity was measured on chondrules and represents a mean field averaged over a cooling timescale of several hours (Fu et al., 2014). The paleointensities for volcanic angrites represent upper limits on the mean external field averaged over a cooling timescale of several days (Wang et al., 2017). The high temperature (HT) magnetization in Kaba represents an upper limit on the mean field averaged over a magnetization acquisition timescale (estimated to range somewhere between 1 y to 1 My). (For interpretation of the colors in the figure, the reader is referred to the web version of this article.)

Wang et al. (2017), this suggests that the nebula itself had dispersed by this time, because current MHD simulations indicate that the presence of nebular gas would support a magnetic field, even in gap regions formed by embedded planets. The lack of a high blocking temperature NRM component in the CV chondrite Kaba confirms that these near-zero field conditions (<0.3 μT) were also present at the CV parent body at 4–6 My after CAI formation. This means that any magnetization acquired later than ∼4 My after CAI formation, including the post-accretional magnetization in CV and H chondrites, is very unlikely be a record of the nebular field. This is consistent with the fact that half of protoplanetary disks around Sun-like YSOs disperse somewhere between ∼2 and 6 My after formation (Bell et al., 2013; Mamajek, 2009). Given that the timescale of acquisition of Allende's magnetization is estimated to be 1–10^4 y assuming it is crystallization remanent magnetization (CRM) or ∼1–10 My assuming it is metamorphic thermoremanent magnetization (TRM), it follows that Allende's ∼60 μT paleointensity is a measure of the field experienced by the body averaged over at least 1 y and perhaps as much as several My. Thus, testing the hypothesis of magnetization by the solar wind should consider the field averaged over these timescales (Section 7).

3. Predicting the solar wind field at the time of Allende magnetization

The solar wind is the extension of the Sun's corona into interplanetary space. This highly conducting plasma flows radially outward, stretching the solar magnetic field and creating the interplanetary magnetic field (IMF). A key factor in testing whether the wind can be responsible for chondrite magnetization is estimating the strength of the IMF at the inferred region of formation of the CV parent body (∼2.5 AU or perhaps further; see, for example, Budde et al., 2016) at the time of magnetization (∼10 My). Direct observations of the speed, density, and magnetic field of stellar winds from other stars at these distances are not available, because stellar winds' low densities do not result in sufficiently strong emission (Wood et al., 2015). On the other hand, the Sun's present-day wind is readily available for direct and continuous observations. Such observations have led to the development of robust theoretical models that can be adapted to the young Sun.

3.1. Our Sun at 10 My

At 10 My after solar system formation, the Sun is expected to be a pre-main sequence T Tauri star, moving along the Hayashi track in the Hertzsprung–Russell diagram toward the main sequence (Kippenhahn et al., 2012). At the start of the Hayashi track, stars are classified as classical T Tauri stars (CTTS), meaning they are surrounded by an accretion disk and/or infalling cloud. Because the meteoritic record shows that the Sun's disk was cleared by ∼4 My after CAI formation (Section 2), the Sun had likely passed the CTTS stage by the time Allende acquired its NRM (∼10 My). On the other hand, the Sun is expected to become a main sequence star only at ∼120 My (Kippenhahn et al., 2012). We can therefore conclude that at the time Allende acquired its NRM, the Sun was likely a weak-line T Tauri star (wTTS) (i.e., a T Tauri star without a disk) and had not yet commenced hydrogen burning.

The identification of the Sun at 10 My as a wTTS has important implications for the type of wind it would have generated. In the CTTS stage, the wind is composed of polar jets, disk winds, and inflow of accreted matter onto the star (Wood et al., 2015). In the absence of the disk, a wTTS will generate a wind similar to the present-day solar wind (i.e., an omnidirectional flow initiated by the thermal pressure gradient between the corona and interplanetary space). The observed properties of solar-like wTTSs at 10 My are listed in Table S3. Of special interest is the average (over the stellar surface) magnetic field of 10–20 mT, which is about ∼100 times larger than the Sun's mean surface field today.

3.2. Analytic description of the IMF

The simplest analytical description of the solar wind is due to Parker (1958), describing a radial transonic flow from a hot corona into interplanetary space. The interplanetary magnetic field, B_{IMF}, at a heliocentric distance, r, has a spiral geometry given by:

$$\mathbf{B}_{IMF} = B_s \left(\frac{R_s}{r} \right)^2 \hat{\mathbf{r}} - B_s \left(\frac{R_s}{r} \right)^2 (r - R_s) \frac{\Omega_\odot \sin\theta}{u_{sw}} \hat{\mathbf{\Phi}} \qquad (1)$$

where $\hat{\mathbf{r}}$ and $\hat{\mathbf{\Phi}}$ are unit vectors in the radial and azimuthal directions, respectively, θ is the polar angle (measured from the polar rotation axis), $\Omega_\odot$ is the radial rotation speed of the Sun, u_{sw} is the terminal wind speed (the asymptotic speed at large distances from the Sun), and B_s and R_s are the reference field magnitude and distance, respectively. The distance R_s is defined as the innermost boundary of the Parker solution (also called the source surface), where the field lines are purely radial by construction. Beyond that distance, all field lines are open and become part of the solar wind. See Table 1 for the symbols used in this manuscript.

The assumptions underlying the Parker derivation should hold for a wTTS of age ∼10 My because the thermal pressure in T Tauri coronae is sufficient for accelerating the wind to supersonic speeds within distances of a few stellar radii (Kiguchi et al., 1998).

3.3. Uncertainties in analytically estimating the IMF of the young Sun

Although the Parker solution is widely used to approximate the present-day IMF, it is not immediately clear how to adjust the parameters u_{sw}, R_s, and B_s to represent the IMF at 10 My: they cannot be directly observed, they are interdependent, and they also depend on the rotation rate, $\Omega_\odot$, which is much faster for the young Sun (see Table S3). In particular, R_s indirectly controls how much of the coronal magnetic field is open and contributes to the IMF (see Section S4 in the Supplementary Material). To overcome these difficulties, we use an MHD model of the corona of a young star (Cohen et al., 2010) that calculates the velocity and magnetic field self-consistently in a rotating frame. As described below, the
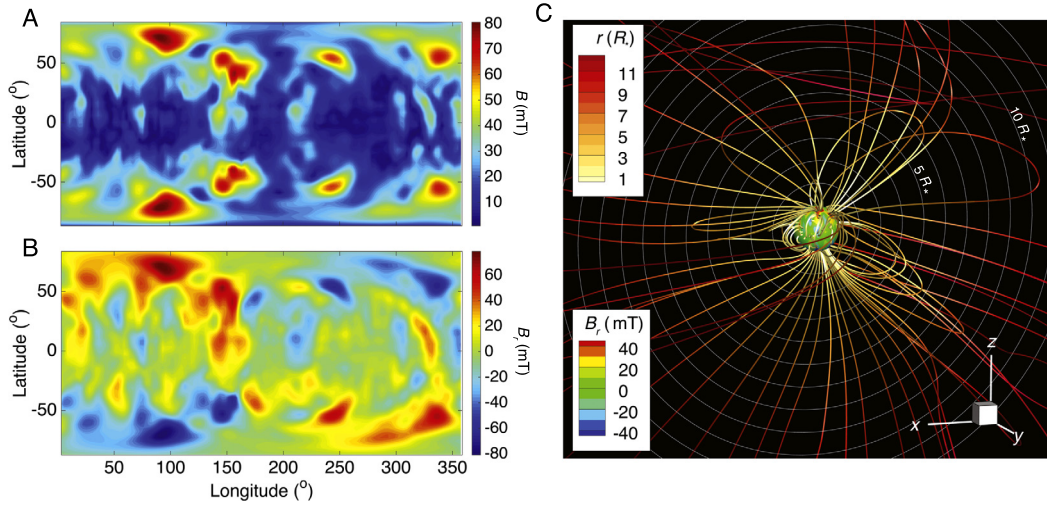
Fig. 2. Observed and modeled field of AB Dor. (A) Total magnitude and (B) radial component of the surface magnetic field obtained from an adjusted ZDI map of AB Doradus taken in December 2007 (data taken from Cohen et al., 2010). The horizontal and vertical axes are the longitude and latitude, respectively. The color contours show field strength. (C) Magnetic field extracted from the MHD solution obtained using the ZDI map. The spherical surface is the stellar surface, colored by the radial magnetic field from the ZDI map. The thick colored curves are magnetic field lines, colored by radial distance from the center. The gray circles mark the radial distance, in units of R_*. (For interpretation of the colors in the figure, the reader is referred to the web version of this article.)

Table 1
Symbols used in this manuscript.

Symbol	Description
R	Asteroid radius
R_*	Stellar radius
$R_\odot$	Solar radius
R_s	Heliocentric distance of source surface
r	Heliocentric radial distance
$\mathbf{B}$, B	Magnetic field vector and magnitude, respectively
B_s	Magnetic field at source surface
B_{IMF}	Interplanetary magnetic field magnitude at 2.5 AU
η	Resistivity of a body
$\mathbf{u}$	Solar wind plasma velocity
u_{sw}	Terminal solar wind speed
ρ	Plasma density
T	Plasma temperature

model is driven by the observed surface magnetic field of a young solar analog and produces a realistic three-dimensional magnetic field topology.

3.4. An MHD model of a young stellar analog AB Doradus

Recent years have seen the development of Zeeman–Doppler Imaging (ZDI) of stellar surfaces (Donati et al., 2006) that provide global maps of surface magnetic fields. These can be combined with the large body of observational and theoretical knowledge about our own solar wind to make predictions about the Sun's early wind. Specifically, several MHD models have been developed that reproduce the large-scale three-dimensional structure of the wind and IMF at 1 AU using surface magnetic field maps as input (most recently in Oran et al., 2013; Meng et al., 2015; Merkin et al., 2016). We use an MHD model of the corona of AB Doradus A (referred to as AB Dor hereafter), a K0 dwarf evolving onto the main sequence (Cohen et al., 2010). The observed stellar properties and those used for the simulation are summarized in Table S3. The model is driven by a ZDI map of AB Dor obtained in December 2007 (see Cohen et al., 2010 for details) (Figs. 2A, B). Although not a G star like the Sun, AB Dor's simulated wind should reasonably approximate that of the Sun at 10 My for the following reasons:

- Both K and G dwarfs are not expected to generate radiatively-driven winds (Abbott, 1982). Instead, their winds, like that of

the Sun, will be driven by thermal pressure and Alfvén waves (Belcher and Olbert, 1975).
- Given AB Dor's mass and radius (Table S3), the gravitational acceleration at its surface would by similar to that of the Sun ($\sim$1.1 $g_\odot$).
- Taking the average of the unsigned flux over the ZDI map of AB Dor yields $<B> = 22.6$ mT. This is consistent with the typical 10–20 mT observed surface magnetic fields of 10 My old wTTSs (Table S3).

The model of AB Dor is implemented within BATS-R-US (Tóth et al., 2012), a three-dimensional highly-parallelized MHD code. Cohen et al. (2010) include three different simulations, named Cases A, B, and C. We use the results from Case A (Fig. 2C) because it is most consistent with a 10 My solar-like star as discussed in Section S5.1 in the Supplementary Material. The model solves the ideal MHD equations and the contribution of Alfvén waves to the wind acceleration is approximated by a variable polytropic index. Although a more consistent treatment of Alfvén waves was incorporated in BATS-R-US in later wind models that were validated at 1 AU and beyond (Oran et al., 2013; Meng et al., 2015; Jin et al., 2011), the polytropic model is also adapted to stellar coronae and was shown to well reproduce the IMF structure of the present-day wind over the entire solar cycle (Cohen et al., 2010).

3.5. Deriving the IMF of AB Dor at 2.5 AU

The AB Dor simulation domain extends up to 45 R_* ($\sim$0.2 AU). Fig. 3 shows the radial velocity and magnetic field in the x–y (equatorial) and the x–z planes. The rotation axis of the star is along the z-axis. The equatorial plots (Figs. 3A, C) reveal a spiral structure created by solar rotation like that described by equation (1). To estimate the IMF magnitude at 2.5 AU, we need to extrapolate the solution from the edge of the computational domain to 2.5 AU using equation (1). If we consider the equatorial plane ($\theta = 0^0$), then the radial component scales as $1/r^2$ while the azimuthal scales as $1/r$. Using $B(r = 45R_*) = 1.2$ μT, and assuming the azimuthal field dominates, the field at 2.5 AU is estimated to be $\sim$90 nT. For simplicity, we take the IMF to be 100 nT as input to the MHD simulations of Section 5, which should be considered an upper limit (see Section S5.1 in the Supplementary Material).
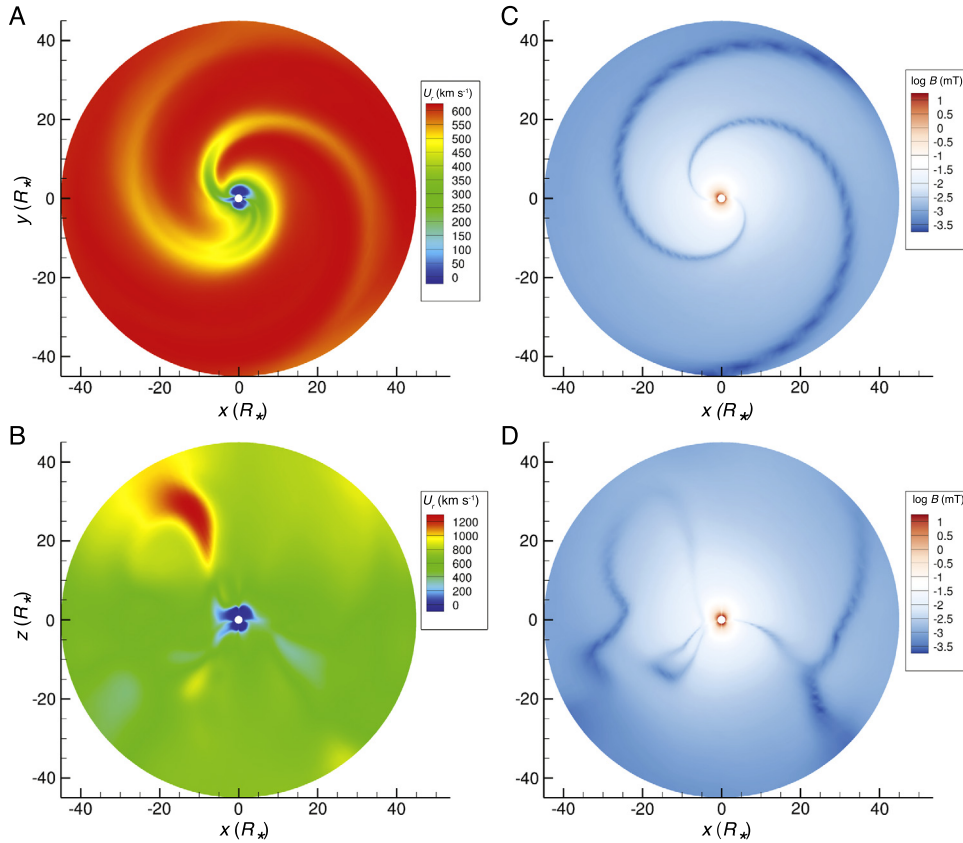
Fig. 3. Output from the AB Dor simulation of Cohen et al. (2010). (A, B) Radial velocity. (C, D) Magnetic field. Data in (A, C) are plotted in the x–y (equatorial) plane (perpendicular to the rotation axis), while data in (B, D) they are plotted in the x–z plane. (For interpretation of the colors in the figure, the reader is referred to the web version of this article.)

4. Theory of solar wind interaction with a chondrite parent body

4.1. Governing equations

The large-scale dynamics of the solar wind can be described by the MHD equations. Here we focus on the magnetic induction equation:

$$\frac{\partial \mathbf{B}}{\partial t} = \nabla \times (\mathbf{u} \times \mathbf{B}) - \frac{\eta}{\mu_0} \nabla^2 \mathbf{B}, \qquad (2)$$

where $\mathbf{B}$ is the magnetic field vector, t is time, $\mathbf{u}$ is the velocity, η is the electric resistivity of the body, and μ_0 is the permeability of free space. The first term on the right hand side represents magnetic field convection with the plasma and the second term on the right hand side describes magnetic diffusion.

4.2. Analytical criteria for magnetic field pile-up

We consider a resistive body is embedded in the solar wind where the magnetic field is perpendicular to the flow direction. Far from the body, $\eta \sim 0$ and the diffusion term in equation (2) can be neglected. Inside the solid body, there is no flow ($\mathbf{u} = 0$) and the convective term vanishes, leaving the field to diffuse inside the body. From dimensional analysis of equation (1), the convection time scale at which the field would flow past a body of size L with speed u is given by:

$$\tau_{conv} = \frac{L}{u}, \qquad (3)$$

while the diffusion time through the body is given by:

$$\tau_{diff} = \frac{\mu_0}{\eta} L^2. \qquad (4)$$

When $\tau_{conv} \ll \tau_{diff}$ (or when $\eta \to 0$), the field around the body would lag behind the free flow, causing field lines to drape and pile-up. This regime describes a flow past an ideal conductor or a body with an ionosphere. A pile-up region was observed around Venus (Kallio et al., 1998), where the magnetic field is enhanced by a factor of 2.5–6.0 (depending on solar wind conditions), and around several comets (e.g., comet 1P/Haley; Israelevich and Ershkovich, 1994) where the magnetic field is enhanced by a factor 2–5.

When $\tau_{conv} \gg \tau_{diff}$ (or when $\eta \to \infty$), the magnetic flux diffuses freely through the body. An example of such a body is the Moon, which acts as an ideal insulator. The diffusion time through the lunar crust is <0.05 s due to its high resistivity [$\sim 10^8$ Ω m; Dyal et al. (1977)]. This is much shorter than the ~ 5 s it takes the wind to flow past the Moon, and no pile-up is created.

It is important to note that a resistive crust can efficiently mask a conducting interior. For example, the lunar mantle is up to 7 orders of magnitude more conducting than the crust (Dyal et al., 1977), implying correspondingly higher diffusion times. Nevertheless, extensive in-situ observations (Zhang et al., 2014) show no detectable pile-up around the Moon. This is an important consequence of diffusion in three dimensions: the crust allows the magnetic field to diffuse around the conducting interior. This effect cannot be captured by two-dimensional simulations: in the absence of a third dimension, the body takes the form of an infinite cylinder such that incoming magnetic flux would continuously pile up in front of conducting layers. In three dimensions, on the other hand, the body constitutes a sphere and the field can slip around it to reach a steady state configuration. Whether or not inner conducting layers would impact the bulk flow of the wind depends on the specific resistivity profile. For the Moon, the upper layers are sufficiently resistive and the highly conducting core

is sufficiently deep such that the conductive interior does not impact the bulk flow of the wind. Regardless of the specific details, all such simulations must be three dimensional unless the body is a perfect insulator and perfect absorber, in which case it does not constitute an obstacle to the flow.

4.3. Estimating the size and resistivity of a chondrite parent body

Although the exact sizes of chondrite parent bodies are not known, meteorite barometry measurements have observed that peak pressures did not exceed 1 kbar (Huss et al., 2006). Assuming hydrostatic equilibrium and a spherical body of uniform density, ρ_0, the central pressure, P_0, is related to the body's radius, R, by:

$$P_0 = \frac{2\pi}{3} G \rho_0^2 R^2, \tag{5}$$

where G is the gravitational constant. The minimal density for C-type asteroids larger than 200 km is 1800 $\mathrm{kg\,m^{-3}}$ (Carry, 2012). For a central pressure of $P_0 = 1$ kbar, this would give a maximal radius of $R \sim 470$ km. This is comparable to Ceres, the largest known asteroid, which has a mean radius of ~476 km (Park et al., 2016).

The resistivity of the CV parent body should have varied with temperature. Assuming a crust at $<300\,°\mathrm{C}$ (the peak metamorphic temperatures for many CV chondrites; Cody et al., 2008) and an interior at $600\,°\mathrm{C}$ (maximum peak metamorphic temperature estimated for CV chondrites; Nagashima et al., 2016) we obtain a resistivity profile that varies between 10^3 and 10^5 $\Omega\,\mathrm{m}$ with radial distance based on temperature-dependent resistivity measurements of Allende presented in Duba and Boland (1984) [note that we selected the measurements done on Duba and Boland (1984)'s Allende sample while it was cooling]. We assume that the thickness of the outer layer of unheated crust is at 0.1–0.05 R, although smaller values are also possible (Sahijpal and Gupta, 2011).

4.4. Will there be a pile-up at a chondrite parent body?

The one-dimensional diffusion timescale through a slab of length 2×470 km with the Allende crustal resistivity is ~10 s. However, diffusion in three dimensions may be up to 3 times faster (Crank, 1979), giving an expected diffusion time of 3–4 s. This is a factor ~2 higher than the convective timescale (~1.3 s for an estimated wind speed of 700 $\mathrm{km\,s^{-1}}$ taken from the AB Dor simulation (Fig. 3)). We conclude that the interaction of a chondrite parent body in the young solar wind constitutes an intermediate case between a Venus-like interaction and a Moon-like interaction, such that only a moderate level of pile-up is expected.

5. Allende in the solar wind: MHD model

5.1. Numerical model

We adapt the BATS-R-US code to solve the ideal MHD equations in regions occupied by the solar wind coupled to the magnetic diffusion equation inside the body. We show that the MHD approximation is justified when considering the IMF at 10 My in Section S1 of the Supplementary Material. The implementation is similar to the Jia et al. (2015) model of the interaction of Mercury's magnetosphere with the solar wind, except that here we model a non-magnetized body that is directly exposed to the wind and lacks a highly conducting core (full details of the numerical implementation are given in Section S2.1 in the Supplementary Material). The body is modeled as a sphere of radius $R = 470$ km (Section 4.3) with a radially varying resistivity: $\eta = 10^5$ $\Omega\,\mathrm{m}$ extending from the center to the base of an outer layer starting at $r = r_{crust}$. For $r > r_{crust}$, η falls logarithmically to 10^3 $\Omega\,\mathrm{m}$ at $r = R$ (see Fig. S2). The body is centered at position $(0, 0, 0)$ and

the solar wind flows in the $-x$ direction. The grid is extended in that direction to contain the wake with dimensions: $x = [-9, 3]$ R, $y = [-4.2, 4.2]$ R, $z = [-4.2, 4.2]$ R. We design a non-uniform spherical grid containing >600,000 cells, with higher resolution in the crust and in the center of the wake where reconnection is expected to occur (see Fig. S2 and Section S2.2 in the Supplementary Material).

The initial condition is that the wind and IMF are both uniform across the body and the magnetic field inside the body is equal to the IMF. Each simulation is run until the pile-up region becomes quasi-static, ensuring the simulation time is longer than the diffusion through the crust (~4 s) and that the solar wind had sufficient time to pass through the domain several times. The typical simulation time ranged between 19 to 24 s, requiring 6–10 hrs on 1200 processors on NASA's Pleiades supercomputer. We note that simulating a true steady state would be too costly (the diffusion time through the conducting layers is 300–1000 s and the time step is ~0.001 s). However, we confirmed that the enhanced field is near-steady by integrating the magnetic field over the entire domain and verifying that the total field magnitude changes by less than <0.2% over time. In any case, the IMF would most likely reverse direction on a scale comparable to an hour or less (Section 7.1) such that the induction process would restart with a different IMF vector, meaning that fully modeling diffusion into the center is unnecessary.

We explore the parameter space with the aim of identifying the solar wind and field configurations that are most favorable for the solar wind magnetization hypothesis. We vary the solar wind conditions (speed, density, and magnetic field direction), as well as the body's internal resistivity profile. The parameter ranges and their justification are summarized in Table S4 and Section S5 of the Supplementary Material.

6. Results

6.1. IMF perpendicular to the wind flow (Cases I and II)

#### Case I: Mean ecliptic wind (baseline case)

The most likely wind parameters at 2.5 AU in the ecliptic plane for the Sun at 10 My were calculated in Section S5 of the Supplementary Material, using the AB Dor simulations as input. These give a speed of ~700 $\mathrm{km\,s^{-1}}$, a density of 35 particles $\mathrm{cm^{-3}}$, and a temperature of 50,000 K (see Table S4). We consider the case where the IMF is perpendicular to the wind flow, pointing in the $+z$ direction, and the wind flows in the $-x$ direction. The body's crust is assumed to be 0.1 R thick. The radial resistivity profile is shown in Fig. S2B. The results are shown in Fig. 4A, which depicts the magnetic field and field lines in a plane containing the wind flow and the IMF (the x–z plane) and the plasma density in the x–y plane. In this case, the magnetic field is enhanced in the upwind side of the body with a maximum field of ~360 nT.

Fig. 5 shows the magnetic field both inside and around the asteroid for the Case I simulation. Selected field lines are also shown. It can be seen that the enhanced magnetic field in the pile-up region is diffusing inside the body around the more conducting interior and emerging in the wake.

Case II: Fast stream, thin crust (most favorable case)

Some wind streams found in the AB Dor simulations are much faster than the typical wind in the ecliptic plane. One such stream can be seen in Fig. 3B, located in the northern hemisphere. Although it does not reach the ecliptic plane (and hence planetary bodies) in this specific magnetic topology, such a stream may well be present in the ecliptic plane at another part of the stellar activity cycle. To model such an event, we set the speed to 1100 $\mathrm{km\,s^{-1}}$ while reducing the initial density to 14 particles $\mathrm{cm^{-3}}$. The lower density is due to the fact that far from the Sun, the wind momentum flux is almost uniform and independent of wind speed
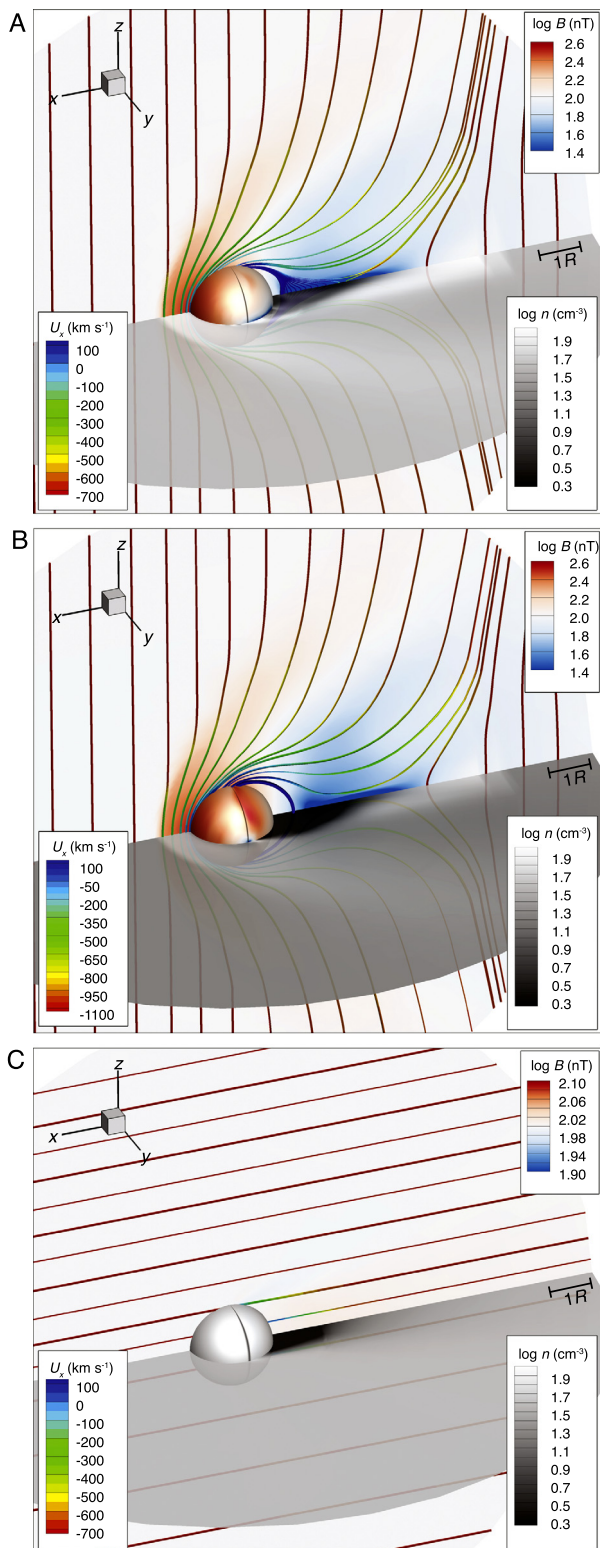
Fig. 4. Simulated magnetic field and density around the asteroid. (A, B, C) Results from Cases I, II, and III, respectively. The wind is flowing from left to right along the −x direction. The red–blue color contours on the meridional (x–z) plane depict magnetic field magnitude. The grayscale contour on the equatorial (x–y) plane depicts the number density. The curves show magnetic field lines and are colored by the velocity in the x direction, demonstrating how the plasma slows down in front of the body and is accelerated down-wind from the reconnection x-point. Note the magnetic field color scale in (C) is narrower than for the other panels because in this configuration (Case III), there is only negligible distortion to the background field due to the body. (For interpretation of the colors in the figure, the reader is referred to the web version of this article.)
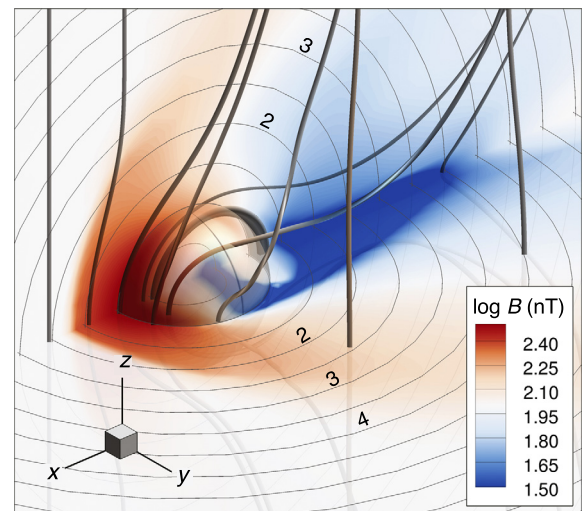

Fig. 5. Magnetic field diffusion in three dimensions, taken from the simulation of Case I at 26 s. The semi-transparent spherical surface marks the surface of the body. Color contours of the magnetic field magnitude are displayed on two perpendicular planes (x–y and x–z). Gray circles mark body-centric radial distances projected on the two planes. The spacings between circles is 1 R. Number labels mark the distance in units of R. The solar wind flows from left to right along the −x axis. Amplification above the initial background field (100 nT) is seen in the upwind side and in the outer shells inside the body, with a maximal field of ∼360 nT. A decrease in field magnitude appears near the center of the body (white and blue regions). The region in blue along the wake axis is a region of field lines disconnected from the wind. The solid curves show selected magnetic field lines. The three lines from the left are solar wind field lines that become increasingly distorted by the body. The four field lines to the right all are passing through the body, demonstrating how the field diffuses around the more conducting interior, and magnetic flux is transported toward the wake region. (For interpretation of the colors in the figure, the reader is referred to the web version of this article.)

(see Supplementary Material Section S5.4). To maximize the level of pile-up the temperature is set to 500,000 K (maximum thermal pressure in Table S4) and the resistivity profile is changed such that the most resistive crust is now only 5% of the entire body. The modified radial resistivity profile is shown in Fig. S2C. In this case, the maximum magnetic field is again ∼360 nT (Fig. 4B). The pile-ups in Cases I and II are similar, demonstrating that the field enhancement is determined by the conversion of kinetic energy into magnetic energy as the wind decelerates. This demonstrates that for a given resistivity profile, the wind speed determines whether a body would be an obstacle, but the wind speed does not uniquely control the level of pile-up due to coupled changes in wind density.

### 6.2. The role of magnetic diffusion through the body and reconnection at the wake

The transfer of magnetic flux through the body into the wake is important because plasmas with anti-parallel fields arrive at the wake axis and create a reconnection region. To examine this, we extracted snapshots at 4 times from the Case II simulation, shown in Fig. 6. The dashed field line in each snapshot marks the field line that passes through the body and reaches the x-point but does not reconnect. More field lines become disconnected from the wind (red curves) as time progresses. The field inside the body diffuses along the outer shell fast, but takes longer to diffuse inwards into the more conducting center. The distance (along the x axis) of the reconnection x-point (marked by the blue vertical line) moves down the wake with time, but eventually settles into an almost fixed position. The diffusion through the body and removal of flux in the wake x-point allows the system to reach a quasi steady state. Although the solar wind brings in more flux, the total magnetic field (integrated over the domain) remains close to constant (less than 0.2% change with time).
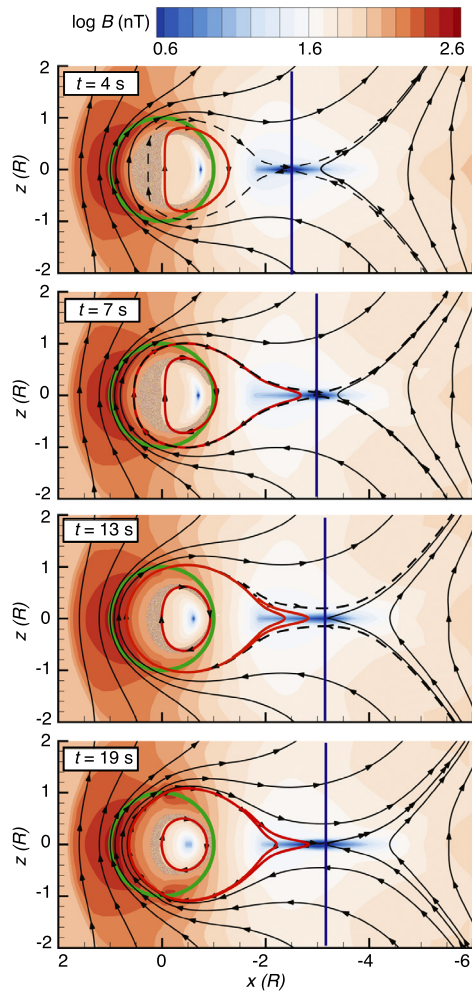
Fig. 6. Magnetic field magnitude and magnetic field lines around the asteroid, extracted at four times during the Case II simulation. The simulation time is marked on the top left corner of each panel. Color contours show the magnetic field in the x–z plane (the plane containing the IMF and the incoming wind flow direction). The green circle outlines the circumference of the body. Solid black curves show the magnetic field lines that are connected to the wind far from the body. The first two field lines from the left in each panel are incoming with the solar wind and show the gradual distortion due to the presence of the body. Other field lines diffuse into the resistive body, and their free edges are dragged by the flow in the $-x$ direction, with each field line reaching closer to the wake axis and the reconnection x-point. The dashed black curve marks the dragged field line that reaches close to the x-point, but does not reconnect. The location of the x-point, where opposite field polarities converge (blue region) changes with time. The vertical blue line marks its location down the wake axis. Downwind from the x-point, reconnected field lines are accelerated outward and rejoin the wind. The field lines within the dashed field lines (solid red) are completely disconnected from wind and are partially inside the body and partially in the wake. In the first few snapshots, they have a significant z component, inherited from the initial background field inside the body. As time progresses, the field diffuses in the outer layers and the magnetic field lines become rounded. The pace at which diffusion progresses around and into the center is demonstrated by the shaded color region inside the body, which is the 100 nT contour (i.e., the initial field level). This region slowly engulfs the center and becomes more rounded and enters deeper into the body. (For interpretation of the colors in the figure, the reader is referred to the web version of this article.)

6.3. IMF parallel to the wind velocity (Case III)

We repeat the same parameters as in Case I, except changing the magnetic field to lie in the x direction. The results (Fig. 4C) show that there is no detectable field enhancement in the upwind side of the body. This behavior is explained by equation (2): the amount of magnetic flux brought in by the wind is proportional to $\mathbf{u} \times \mathbf{B}$ and thus in this configuration there is no new flux to be piled-up.
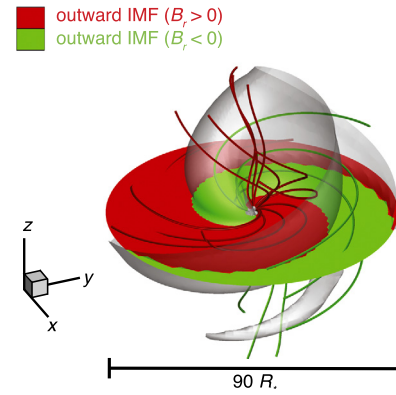
Fig. 7. The inferred magnetic field polarity of AB Dor. The domain shown covers a radius of 45 R_*. The slice lying in the x–y plane is colored by the sign of the radial magnetic field, where green and red signify outward and inward pointing field lines, respectively. The curves show selected magnetic field lines extracted within the domain, colored by the same color code. The semi-transparent gray surface signifies the location of the current sheet, where B_r equals to zero (i.e., the field reverses sign). The spiraling of the field lines and warping of the current sheet away from the ecliptic plane are the result of the rotation of the star and the non-axisymmetric dynamo field (see Fig. 2). (For interpretation of the colors in the figure, the reader is referred to the web version of this article.)

6.4. Summary

In contrast to the present-day Moon, a warm chondritic body is capable of distorting the upwind field because its resistivity is 3 orders of magnitude smaller than that of the lunar crust. However, even the case of strongest possible interaction produces a field enhancement of only a factor of 3.6. By comparison, Venus generates a factor of ~6 enhancement under the much lower ram pressure of the present-day wind (Kallio et al., 1998) due to its highly conducting ionosphere. We tested the robustness of the above conclusion by varying the radius of the body (250 km and 340 km). The results were qualitatively the same, but with lower compression factors, as expected from our discussion of parameter space (Supplementary Material and Table S4). For the present-day wind conditions (speed of 400 km s^{-1} and IMF of 5 nT), the asteroid only caused a factor of 1.5 enhancement.

Another analogous body is Ceres, which is of similar size to the CV parent body assumed here. Hybrid simulations of Ceres in the present-day wind estimate the field enhancement at this body to be a factor 2 (Lindkvist et al., 2017). Ceres is thought to be more resistive than the CV parent body assumed here and it is therefore expected that the enhancement would be lower. Although there are some important differences between Ceres and the CV body, namely that Ceres emits vapor and its interaction is somewhat analogous to a comet, the simulations of Lindkvist et al. (2017) show that the field values obtained here are broadly consistent with those of other bodies.

7. Mean pile-up field over the magnetization timescales

7.1. Systematic periodicities in the IMF

A critical quantity relevant to parent body magnetization by the solar wind is the mean field experienced by the body over the NRM acquisition timescale. The present-day IMF is highly directionally variable and turbulent (Fig. S3). In particular, there are two important large-scale periodicities that will affect the magnetization of a planetary body:

- IMF sectors: The field lines making up the IMF have alternating polarities depending on where the lines originate on the Sun's surface. A current sheet separates regions of opposite polarity and rotates with the Sun (presently with a period of
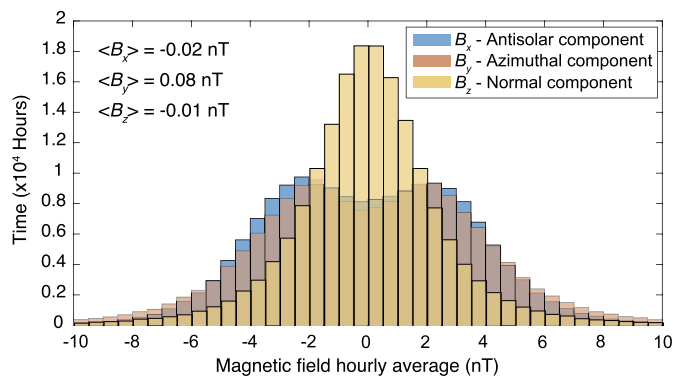
Fig. 8. Temporal variation of the solar wind. Shown is a histogram of hourly averages of IMF vector components measured in the solar wind at 1 AU, over a 22 y period from February 1995 to February 2017, equivalent to a full solar cycle. The blue, orange and yellow data denote the x, y, and z field components, respectively, in the GSE system (Supplementary Material). Data taken from OMNI, a cross-spacecraft calibrated dataset of in-situ solar wind measurements at 1 AU (King and Papitashvili, 2006), available through NASA's CDAWeb. The magnetic field in each hour interval was averaged and averages were binned in 0.5 nT intervals. (For interpretation of the colors in the figure, the reader is referred to the web version of this article.)

∼25 days). This structure is shown in Fig. 7 for the AB Dor simulation.

- The solar cycle: Solar activity and the solar magnetic field vary on a 22-y solar cycle. At solar minimum the magnetic field is largely dipolar and the dipole axis flips between two consecutive minima (i.e., every 11 y).

The effects of these periodicities can be examined quantitatively using in-situ solar wind measurements taken near Earth's orbit. Fig. 8 shows the distribution of hourly averages of IMF components over 22 y (1995–2007). The components in the x, y, and z directions are measured in the Geostationary-Ecliptic (GSE) system (see Section S3 in the Supplementary Material). The distribution of each component is almost perfectly symmetric, with the mean of the x, y, and z components being −0.02, 0.08, and −0.01 nT, respectively (about a factor of 100 less than the instantaneous magnitude of 2–10 nT). Detailed analysis (Supplementary Material and Fig. S4) shows that this effect is already present when averaging over a solar rotation (∼25 days), since the Earth spends similar amounts of time in opposite-polarity regions due to the rotating IMF sectors.

Furthermore, Case III demonstrated that there is little to no enhancement when the field is parallel to the velocity. Since the IMF may take many different directions, the ideal configuration will only occur for part of the time (Fig. S5).

We expect the long-term behavior of the IMF at 10 My to be similar except that the Sun at 10 My would have a shorter rotation period of 0.5–2 days (Table S3), meaning field reversals due to IMF sectors are expected to occur several times a day. The faster rotation also implies a shorter solar cycle of 2–5 y or less (Metcalfe et al., 2016).

7.2. An upper limit of the mean pile-up field

The field experienced by the chondrite parent body would be at the most 360 nT for short periods of time (∼hours). This should be considered as an extreme upper limit, since it was obtained by setting all free parameters to values associated with the most favorable case:

- The highest estimate of the young Sun's surface field from astronomical observations of similarly aged stars (Section 3.1).
- The upper limit for the IMF at 2.5 AU, based on self-consistent modeling of the wind driven by an observed ZDI map of a pre-main sequence star (Section 3.4 and Supplementary Material).

- The upper limit for the solar wind ram pressure at 2.5 AU (Section 3.4 and Supplementary Material).
- Largest body and thinnest crust (Section 4.3).
- Most favorable configuration of the IMF angle with respect to the flow (Section 6).
- Considering temporal averaging due to observed IMF reversals, that were more frequent at 10 My (Section 7.1).

Under the well-established and systematic periodicities on the IMF, the average IMF component over the solar cycle is a factor of 100 less than the instantaneous field. Thus, the mean field recorded by parent bodies (given the 1 y–1 My acquisition times of meteorite NRM; Section 2) should be at least a factor of 100 lower, or just <3.5 nT. The mean enhanced field is therefore at least 10^3 and 10^4 too small to explain the magnetization of Kaba and Allende, respectively (Table S2). Even if Allende's paleointensity was only several ∼6 μT instead of ∼60 μT (as recently suggested by Muxworthy et al., 2017), the instantaneous and mean solar wind fields would still be ∼20 and ∼2000 times too weak to account for Allende's NRM.

8. Conclusions

- We presented the first numerical simulations of the interaction of the solar wind with a resistive, non-magnetized, and airless asteroid for which the field evolution is controlled by magnetic diffusion in the interior. We showed that when such a body has the electrical resistivity of a hot undifferentiated chondrite, it does not constitute a significant obstacle to the wind flow.
- The field is compressed only up to a factor of ∼3.6 at the body under the most favorable instantaneous conditions, leading to an instantaneous field of only ≤360 nT, which is 10 and 100 times below most paleointensity estimates for Kaba and Allende, respectively.
- Our analysis of IMF temporal variations shows that even the optimal configuration would be short-lived (persisting for a timescale of an hour) and may be rapidly followed by an IMF in the opposite direction. We argued from analytical time scale analysis that changes in the IMF would wash over the entire body over these timescales.
- Statistical analysis of the present-day solar wind shows the IMF averaged over timescales of years is a 100 times weaker than instantaneous values. Because the existence of IMF sectors and solar activity are well established for T Tauri stars, it is reasonable to assume similar periodicities existed in the young solar wind. This implies the mean amplified field induced in the body would be at least 10^3–10^4 times below the paleointensities typically estimated for Kaba and Allende, respectively.
- Eliminating the solar wind as a source of magnetization supports the alternative hypothesis that the paleomagnetic record is a record of a core dynamo. Despite being primitive materials, chondrites may be samples of a partially differentiated body (Weiss and Elkins-Tanton, 2013).

Appendix A. Supplementary material

Supplementary material related to this article can be found online at https://doi.org/10.1016/j.epsl.2018.02.013.

References

Abbott, D.C., 1982. The theory of radiatively driven stellar winds. II – The line acceleration. Astrophys. J. 259, 282–301.

Belcher, J.W., Olbert, S., 1975. Stellar winds driven by Alfven waves. Astrophys. J. 200, 369–382.

Bell, C.P.M., Naylor, T., Mayne, N.J., Jeffries, R.D., Littlefair, S.P., 2013. Pre-mainsequence isochrones? II. Revising star and planet formation timescales. Mon. Not. R. Astron. Soc. 434, 806–831.

Bryson, J.F.J. Weiss, B.P. Scholl, A. Getzin, B.L. Abrahams, J.N.H. Nimmo, F., 2016. Paleomagnetic evidence for a partially differentiated H chondrite parent planetesimal. Abstract P53D-02 presented at 2016 Fall Meeting, AGU, San Francisco, Calif., 11–15 Dec.

Budde, G., Kleine, T., Kruijer, T.S., Burkhardt, C., Metzler, K., 2016. Tungsten isotopic constraints on the age and origin of chondrules. Proc. Natl. Acad. Sci. 113, 2886–2891.

Carporzen, L., Weiss, B.P., Elkins-Tanton, L.T., Shuster, D.L., Ebel, D.S., Gattacceca, J., 2011. Magnetic evidence for a partially differentiated carbonaceous chondrite parent body. Proc. Natl. Acad. Sci. USA 108, 6386–6389.

Carry, B., 2012. Density of asteroids. Planet. Space Sci. 73, 98–118.

Cody, G.D., Alexander, C.M., Yabuta, O'D.H., Kilcoyne, A.L.D., Araki, T., Ade, H., Dera, P., Fogel, M., Militzer, B., Mysen, B.O., 2008. Organic thermometry for chondritic parent bodies. Earth Planet. Sci. Lett. 272, 446–455.

Cohen, O., Drake, J.J., Kashyap, V.L., Hussain, G.A.J., Gombosi, T.I., 2010. The coronal structure of AB Doradus. Astrophys. J. 721, 80–89.

Connelly, J.N., Bizzarro, M., Krot, A.N., Nordlund, Å., Wielandt, D., Ivanova, M.A., 2012. The absolute chronology and thermal processing of solids in the solar protoplanetary disk. Science 338, 651–655.

Cournède, C., Gattacceca, J., Gounelle, M., Rochette, P., Weiss, B.P., Zanda, B., 2015. An early solar system magnetic field recorded in CM chondrites. Earth Planet. Sci. Lett. 410, 62–74.

Crank, J., 1979. The Mathematics of Diffusion. Oxford University Press, p. 414.

Desch, S.J., Mouschovias, T.Ch., 2001. The magnetic decoupling stage of star formation. Astrophys. J. 550, 314–333.

Donati, J.F., Howarth, I.D., Jardine, M.M., Petit, P., Catala, C., Landstreet, J.D., Bouret, J.C., Alecian, E., Barnes, J.R., Forveille, T., Paletou, F., Manset, N., 2006. The surprising magnetic topology of τ Sco: fossil remnant or dynamo output? Mon. Not. R. Astron. Soc. 370, 629–644.

Duba, A.G., Boland, J.N., 1984. High temperature electrical conductivity of the carbonaceous chondrites Allende and Murchison. In: Proc. Lunar Planet. Sci. Conf. 15, pp. 232–233.

Dyal, P., Parkin, C.W., Daily, W.D., 1977. Lunar Electrical Conductivity, Permeability and Temperature from Apollo Magnetometer Experiments. NASA Special Publication 370.

Elkins-Tanton, L.T., Weiss, B.P., Zuber, M.T., 2011. Chondrites as samples of differentiated planetesimals. Earth Planet. Sci. Lett. 305, 1–10.

Fu, R.R., Weiss, B.P., Lima, E.A., Harrison, R.J., Bai, Xue-Ning, Desch, S.J., Ebel, D.S., Suavet, C., Wang, H., Glenn, D., Le Sage, D., Kasama, T., Walsworth, R.L., Kuan, A.T., 2014. Solar nebula magnetic fields recorded in the Semarkona meteorite. Science 346, 1089–1092.

Gattacceca, J., Weiss, B.P., Gounelle, M., 2016. New constraints on the magnetic history of the CV parent body and the solar nebula from the Kaba meteorite. Earth Planet. Sci. Lett. 455, 166–175.

Huss, G.R., Rubin, A.E., Grossman, J.N., 2006. Thermal metamorphism in chondrites. In: Lauretta, D.S., McSween, H.Y. (Eds.), Meteorites and the Early Solar System II. University of Arizona Press, Tucson, pp. 567–586. 943 pp.

Israelevich, P.L., Ershkovich, A.I., 1994. Induced magnetosphere of comet Halley. 2: Magnetic field and electric currents. J. Geophys. Res. 99, 21.

Jia, X., Slavin, J.A., Gombosi, T.I., Daldorff, L.K.S., Toth, G., van der Holst, B., 2015. Global MHD simulations of Mercury's magnetosphere with coupled planetary interior: induction effect of the planetary conducting core on the global interaction. J. Geophys. Res. 120, 4763–4775.

Jin, M., Manchester, W.B., van der Holst, B., Gruesbeck, J.R., Frazin, R.A., Landi, E., Vasquez, A.M., Lamy, P.L., Llebaria, A., Fedorov, A., Toth, G., Gombosi, T.I., 2011. A global two-temperature corona and inner heliosphere model: a comprehensive validation study. Astrophys. J. 745, 1.

Kallio, E., Luhmann, J.G., Lyon, J.G., 1998. Magnetic field near Venus – a comparison between Pioneer Venus Orbiter magnetic field observations and an MHD simulation. J. Geophys. Res. 103, 4723.

Kataoka, K., Muto, T., Momose, M., Tsukagoshi, T., Fukagawa, M., Shibai, H., Hanawa, T., Murakawa, K., Dullemond, C.P., 2015. Millimeter-wave polarization of protoplanetary disks due to dust scattering. Astrophys. J. 809, 78.

Kiguchi, M., Narita, S., Hayashi, C., 1998. Wind from T Tauri stars. Publ. Astron. Soc. Jpn. 50, 587–595.

King, J., Papitashvili, N., 2006. 5 minute averaged definitive multispacecraft interplanetary parameters data (OMNI_HRO_5MIN). Available on NASA CDAWeb: https://cdaweb.sci.gsfc.nasa.gov.

Kippenhahn, R., Weigert, A., Weiss, A., 2012. Stellar Structure and Evolution, second edition. Springer-Verlag, Berlin. 604 pp.

Kivelson, M.G., Russell, C.T., 1995. In: Kivelson, Margaret G., Russell, Christopher T. (Eds.), Introduction to Space Physics. Cambridge University Press, p. 586.

Klein, B.Z., Weiss, B.P., Carporzen, L., 2014. More evidence for a partially differentiated CV chondrite parent body from paleomagnetic studies of ALH 84028 and ALH 85006. Abstract GP51B-3736 presented at 2014 Fall Meeting, AGU, San Francisco, Calif., 15–19 Dec.

Lindkvist, J., Holmström, M., Fatemi, S., Wieser, M., Barabash, S., 2017. Ceres interaction with the solar wind. Geophys. Res. Lett. 44, 2070–2077.

Mamajek, E.E., 2009. Initial conditions of planet formation: lifetimes of primordial disks. In: Usuda, T., Ishii, M., Tamura, M. (Eds.), Exoplanets and Disks: Their Formation and Diversity, vol. 1158, pp. 3–10.

Meng, X., van der Holst, B., Tóth, G., Gombosi, T.I., 2015. Alfvén wave solar model (AWSoM): proton temperature anisotropy and solar wind acceleration. Mon. Not. R. Astron. Soc. 454, 3697–3709.

Merkin, V.G., Lionello, R., Lyon, J.G., Linker, J., Török, T., Downs, C., 2016. Coupling of coronal and heliospheric magnetohydrodynamic models: solution comparisons and verification. Astrophys. J. 831 (23), 23.

Metcalfe, T., Egeland, R., van Saders, J., 2016. Stellar evidence of a solar dynamo in transition. In: 19th Cambridge Workshop on Cool Stars, Stellar Systems, and the Sun (CS19), p. 28.

Muxworthy, A.R., Bland, P.A., Davison, T.M., Moore, J., Collins, G.S., Ciesla, F.J., 2017. Evidence for an impact-induced magnetic fabric in Allende, and exogenous alternatives to the core dynamo theory for Allende magnetization. Meteorit. Planet. Sci., 1945–5100.

Nagashima, K., Krot, A.N., Komatsu, M., 2016. ^{26}Al–^{26}Mg systematics in chondrules from Kaba and Yamato 980145 CV3 carbonaceous chondrites. Geochim. Cosmochim. Acta 201, 303–319.

Nagata, T., 1979. Meteorite magnetism and the early solar system magnetic field. Phys. Earth Planet. Inter. 20, 324–341.

Oran, R., van der Holst, B., Landi, E., Jin, M., Sokolov, I.V., Gombosi, T.I., 2013. A global wave-driven magnetohydrodynamic solar model with a unified treatment of open and closed magnetic field topologies. Astrophys. J. 778, 176.

Park, R.S., Konopliv, A.S., Bills, B.G., Rambaux, N., Castillo-Rogez, J.C., Raymond, C.A., Vaughan, A.T., Ermakov, A.I., Zuber, M.T., Fu, R.R., Toplis, M.J., Russell, C.T., Nathues, A., Preusker, F., 2016. A partially differentiated interior for (1) Ceres deduced from its gravity field and shape. Nature 537 (7621), 515–517.

Parker, E.N., 1958. Dynamics of the interplanetary gas and magnetic field. Astrophys. J. 128, 664.

Sahijpal, S., Gupta, G., 2011. Did the carbonaceous chondrites evolve in the crustal regions of partially differentiated asteroids? J. Geophys. Res. 116, E06004.

Scheinberg, A., Fu, R.R., Elkins-Tanton, L.T., Weiss, B.P., 2015. Asteroid differentiation: hydrous and silicate melting and large-scale structure. In: Michel, P., DeMelo, F., Bottke, W.F. (Eds.), Asteroids IV. University of Arizona Press, pp. 533–552.

Shah, J., Bates, H.C., Muxworthy, A.R., Hezel, D.C., Russell, S.S., Genge, M.J., 2017. Long-lived magnetism on chondrite parent bodies. Earth Planet. Sci. Lett. 475C, 106–118.

Stephens, I.W., Looney, L.W., Kwon, W., Fernández-López, M., Hughes, A.M., Mundy, L.G., Crutcher, R.M., Li, Z.Y., Rao, R., 2014. Spatially resolved magnetic field structure in the disk of a T Tauri star. Nature 514, 597–599.

Tarduno, J.A., O'Brien, T.M., Blackman, E.G., Smirnov, A.V., 2017. Magnetization of CV meteorites in the absence of a parent body core dynamo. In: Proc. Lunar Planet. Sci. Conf., 48, p. 2850.

Tóth, G., van der Holst, B., Sokolov, I.V., De Zeeuw, D.L., Gombosi, T.I., Fang, F., Manchester, W.B., Meng, X., Najib, D., Powell, K.G., Stout, Q.F., Glocer, A., Ma, Y., Opher, M., 2012. Adaptive numerical algorithms in space weather modeling. J. Comput. Phys. 231 (3), 870–903.

Wang, H., Weiss, B.P., Bai, X.N., Downey, B.G., Wang, J., Wang, J., Suavet, C., Fu, R.R., Zucolotto, M.E., 2017. Lifetime of the solar nebula constrained by meteorite 121 paleomagnetism. Science 355, 623–627.

Weiss, B.P., Elkins-Tanton, L.T., 2013. Differentiated planetesimals and the parent bodies of chondrites. Annu. Rev. Earth Planet. Sci. 41, 529–560.

Weiss, B.P., Wang, H., Sharp, T.G., Gattacceca, J., Shuster, D.L., Downey, B., Hu, J., Fu, R.R., Kuan, A.T., Suavet, C., Irving, A.J., Wang, J., Wang, J., 2017. A nonmagnetic differentiated early planetary body. Earth Planet. Sci. Lett. 468, 119–132.

Wood, B.E., Linsky, J.L., Gudel, M., 2015. Stellar winds in time. In: Lammer, H., Khodachenko, M. (Eds.), Characterizing Stellar and Exoplanetary Environments. In: Astrophysics and Space Science Library, vol. 41, pp. 19–35.

Zhang, H., Khurana, K.K., Kivelson, M.G., Angelopoulos, V., Wan, W.X., Liu, L.B., Zong, Q.G., Pu, Z.Y., Shi, Q.Q., Liu, W.L., 2014. Three-dimensional lunar wake reconstructed from ARTEMIS data. J. Geophys. Res. Space Phys. 119, 5220–5243. https://doi.org/10.1002/2014JA020111.

Supplementary Material for
Were Chondrites Magnetized by the Early Solar Wind?

Oran, R.*, Weiss, B. P., Cohen, O.

Earth and Planetary Science Letters

* Corresponding author. Email: roran@mit.edu

This PDF file includes:

Supplementary Text
Supplementary Figures
Supplementary Tables
Supplementary References

Supplementary Text and Figures

1. Justifying the magnetohydrodynamic (MHD) approximation

The interaction of the solar wind with small bodies like asteroids is commonly modeled using hybrid simulations (where electrons are treated as a fluid and ions as particles) since the ion gyroradius is of the order of the size of the body for the present-day solar wind (Omidi et al., 2002; Simon et al., 2006; Fatemi et al., 2018). These studies modeled magnetized asteroids for which magnetic diffusion inside the body was either not included or its effects were negligible. Fatemi et al. (2018) also considered a case of a non-magnetized asteroid with high electric conductivity, in which case the solar wind magnetic field was essentially excluded from the interior in the timescale of the simulation. The effects of resistivity were previously included in simulations of larger bodies like Mercury using an MHD model (Jia et al., 2015), and for the Moon using hybrid codes (Wang et al., 2011; Fatemi et al., 2017). The latter two cases present limiting cases: a large magnetized obstacle (Mercury) and an almost ideal insulator that does not deflects the wind (the Moon).

The simulations in the present work aim to simulate a distinctly different type of interaction, one where the body is non-magnetized and airless, and neither an ideal insulator nor an ideal conductor. The interaction region of such a body is largely shaped by the rate at which the magnetic field can diffuse into the body as the wind flows past it (see analytical derivation in Section 4 in the main text). To our knowledge, these simulations, first presented in Oran & Weiss (2017) and expanded for the present work, are the first simulations of the solar wind interaction with a resistive asteroid which resolve and are largely controlled by diffusive processes in the interior.

As discussed in Section 4 in the main text, diffusion through the outer, most resistive layer of the CV chondrite parent body is a key factor that controls how much the solar wind field would be enhanced in the pile-up region. To resolve this process in the crust (which has a thickness of $\sim$10% of the body's radius; see Section 4.3 in the main text), we require cell sizes of $\sim$1-2% of the body's radius. MHD modeling has the advantage over hybrid modeling in this scenario because they are less computationally expensive and thus allow for smaller cell sizes (we compare the cell sizes realized in the present MHD simulations to those used in previously published hybrid simulations in Section S2.2.1). However, to justify using an MHD code, we

must first ensure that this approximation is valid for simulating a small body in the ancient solar wind.

For the present-day solar wind, the ion gyroradius is 100-200 km given an interplanetary magnetic field (IMF) of ∼2 nT at the asteroid belt. This requires the use hybrid models of asteroids discussed above. In contrast, the present study is focused on the ancient IMF that is 50 times larger than the present-day value, giving an ion gyroradius that is only 2-4 km (all other parameters being equal). This is two orders of magnitude smaller than the radius of the CV chondrite parent body considered here (∼470 km; see derivation in Section 4.3 in the main text). Therefore, an MHD model should adequately capture the interaction including the level of magnetic field pile-up in front of the body.

We note that kinetic effects will be mostly important in the wake and may produce specific wave modes that are not accessible to MHD (Wang et al., 2011), but these details should not have a significant effect on the global structure of the interaction. To confirm this, we performed an ideal three dimensional (3D) MHD simulation of Ceres' interaction with the present-day wind and compared it to a published 3D hybrid simulation (Kallio et al., 2008). Ceres's radius is similar to that of the CV parent body assumed in the present study (see Section 4.3 in the main text). We used the same solar wind conditions, domain size, and body size as the hybrid model. We assumed the body is an ideal absorber and a very good insulator (with a uniform resistivity of 10^7 Ω m^{-1}, similar to that of the lunar crust), while in the hybrid simulation the body was treated as an ideal absorber and ideal insulator. The comparison of the two models is shown in Fig. S1. The top panel is the MHD result, while the bottom panel is adapted from Fig. 1 in Kallio et al. (2008). We find that the large scale structure of the wake predicted by the MHD simulation is consistent with the hybrid model result. Although finer details inside the wake do differ, this demonstrates that the overall steady-state structure is well-reproduced by MHD for a body of this size, even for present-day solar wind conditions.

The actual size of the parent body is not known and indeed might be smaller than the model body chosen here, in which case a hybrid or even full kinetic code might be appropriate. However a smaller asteroid will have a weaker interaction with the solar wind and will create a smaller compression of the incoming IMF. Since we seek to obtain an upper limit on the pile up field, the small parent body case is not of interest to the present work.
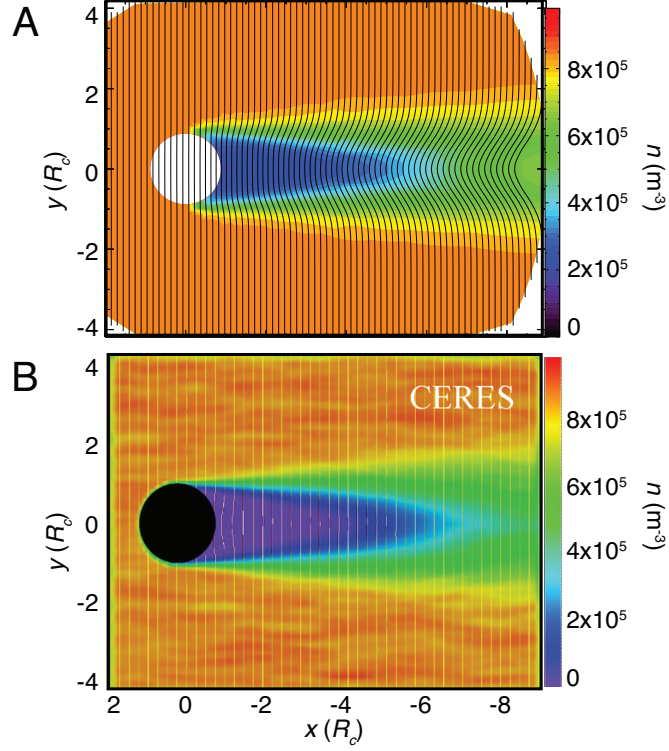
Fig. S1. Ceres' interaction with the solar wind. (A) An ideal MHD simulation (this study). (B) A hybrid simulation adapted from Fig. 1 in Kallio et al. (2008). Results are plotted in the x-y plane (the solar wind flows from the left). Distances are given in Ceres radii, R_c. Color contours show the particle density and curves show magnetic field lines. The range of values represented by the color scale for both plots is the same, but the color maps are slightly different. The white and black circles show the asteroid body in the top and bottom panel, respectively. In the MHD model, the body was included in the simulation domain (with an assumed high electric resistivity, see text), while in the hybrid simulation the body was excluded from the domain and a boundary condition of an ideal insulator was applied at the surface.

4

2. Numerical model of a resistive body in the solar wind

In the present work, we solve two different sets of equations in different parts of the simulation domain. Inside the body, there is no plasma and the magnetic field evolves according to magnetic diffusion as described by the induction equation (equation 2 in the main text). Outside the body, the plasma is treated as a perfectly conducting fluid governed by the ideal MHD equations, for which diffusive effects are negligible. To simulate both regimes using an MHD code, we employ a method similar to that presented in Jia et al. (2015), who modeled the body as a solid by suppressing the flow in that part of the domain but allowing the magnetic field to evolve due to diffusion. Jia et al. (2015) applied this approach within the Block-Adaptive-Tree-Solarwind-Roe-Upwind-Scheme (BATS-R-US; Tóth et al., 2012) code to simulate Mercury's magnetosphere. Our implementation, also within the BATS-R-US code, is slightly different, as the chondritic body is not magnetized, is directly exposed to the solar wind, and does not have a core. The simulation domain includes two boundaries: an outer boundary far from the body in the solar wind, and a boundary at the interface between the body and the wind. In the interior, the domain extends to the center of the body. The physical boundary conditions at the interface are that the magnetic field is allowed to diffuse past it, while plasma flowing onto the interface is absorbed, and there is no flow on the interior side.

2.1. Simulating a resistive solid with the BATS-R-US code

2.1.1. Utilizing the block structure

BATS-R-US is a finite-volume code based on a block-tree grid structure: the computational domain is first divided into blocks, and each block is made up of a fixed structure of cells. In the current implementation, we use a spherical grid organized into computational blocks of $6\times4\times4$ cells in the r, Φ, and θ directions (representing the radial, azimuthal, and polar directions, respectively). The grid can be refined in regions where strong gradients in the solution occur while keeping cell sizes large where the solution is smooth. A block that is to be refined is divided into 8 daughter blocks of identical cell structure (by dividing the original block volume along each of the three spatial dimensions). Refinement is performed in successive steps until the desired spatial size of the cells is achieved. Thus even though each block may represent a different spatial volume depending on its location in the spherical domain and on the level of grid refinement, the algorithm for updating the

solution in each block is identical. This approach simplifies grid refinements and parallelizing the code across many processors. Further details about the BATS-R-US grid refinement procedures can be found in (Tóth et al., 2012).

The block structure allows us to easily separate the domain and solve separate equations, provided that the boundary between the body and the wind aligns with block edges. This is easily achieved in the spherical grid used in this work by designing a grid where $r = 1R$ coincides with a block edge in the radial direction (where R is the body radius). All the blocks with $r \leq R$ are body blocks and those with $r > R$ are solar wind blocks. The use of a spherical grid does carry a price that the cells near the poles of the grid become increasingly small, limiting the time step. Furthermore, since BATS-R-US is a finite-volume code that updates the solution by calculating the fluxes through cell faces, some difficulty arises in the cells that lie exactly on the polar axis (i.e. that have one face with zero area). To overcome this, BATS-R-US employs the supercell algorithm for which the solution update in polar cells is modified to take into account all the cells around the pole. The algorithm is described in detail in Tóth et al. (2012).

2.1.2. Applying boundary conditions at the body's surface.

Each computational block is surrounded by 2 layers of ghost cells in each direction, which partially overlap with neighboring blocks. At the beginning of each time step, the information from the neighboring blocks is interpolated into the ghost cells and solution is advanced inside the block. The ghost cell design allows us effectively create an interface between the resistive body and the solar wind: by modifying the information in the ghost cells of blocks on both sides on the body's surface, we can impose boundary conditions that describe a resistive absorbing body. In the present model, we set the following boundary conditions:

- For solar wind blocks, the density, velocity, and pressure in the ghost cells that overlap the body are overwritten to impose absorbing boundary conditions for the wind.

- For body blocks, the ghost cells that overlap the exterior are filled with fixed density and pressure as in all the body cells, and a zero velocity is imposed.

- The magnetic field components in all cells are not modified, allowing for magnetic energy to diffuse between the exterior and the interior.

2.2. Computational grid design for resistive asteroids

The 6×4×4 block design allows for more resources to be diverted to the radial direction and to better resolve the crust. The body is centered at position $(0, 0, 0)$ and extends up to a radial distance of $1R$. The grid dimensions are $x = $ [-9.0, 3.0] R, $y = $ [-4.2, 4.2] R, $z = $ [-4.2, 4.2] R. The basic grid (before refinement) is divided into 4 blocks along each of the spherical grid dimensions, giving a total of 64 blocks. The baseline radial spacing is 0.1875 R. The grid is refined at regions where sharp gradients are expected. Since refinement is achieved by cutting blocks in half in each dimension, resolution changes occur at jumps of factors 2 between neighboring blocks. This minimizes discretization errors while saving on computational resources in regions where the solution is smooth. Two regions of interest are the highly resistive crust and the wake region. After these regions are refined as described below, the grid comprises 6,414 blocks and >600,000 cells. The final grid is shown in Fig. S2.
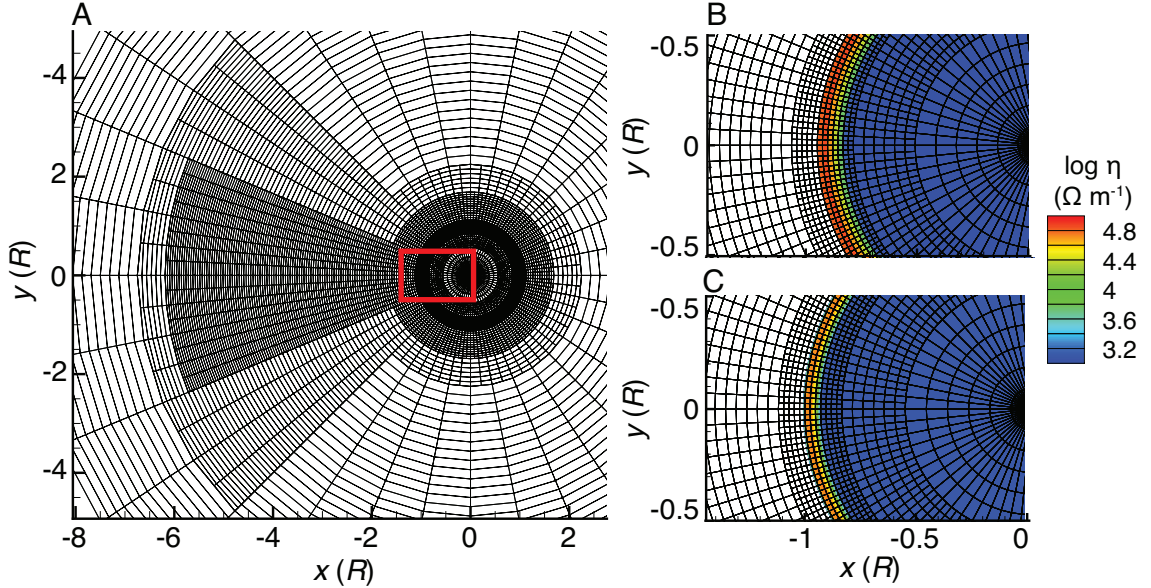
Fig. S2. (A) Numerical grid used for simulating the interaction of the solar wind with a resistive CV parent body. Shown is a two-dimensional cut in the x-y plane, demonstrating the refinement in the crust and wake regions. The red box denotes the part of the grid shown in (B) and (C). The axes are measured in units of body radii, R. (B) Radial profile of the resistivity used Case I and Case III in red boxed region in (A) (see Section 6). The color contours show the resistivity and black curves show the grid. (C) Same as (B) but for Case II, which possesses a thinner crust.

2.2.1. Crust refinement

The crust is defined as a spherical shell between 0.9 R to 1 R. Because the crust is the most resistive part of the body, magnetic diffusion is fastest there. To improve accuracy, we need to minimize the numerical diffusion in this region, which is proportional to dr^2, where dr is the cell size in the radial direction. The grid refinement level in the crust is 4 (where level 1 represents the baseline grid), meaning that each block that overlaps the crust is divided in half 4 consecutive times. The crust cells have a radial extent $dr \sim 0.023$ R inside this layer. We tested whether resolving the crust by a further level of refinement (level 5, with $dr \sim 0.011$ R) changes the level of compression in the pile-up region, but observed no significant change in the global structure for a test run on a smaller domain. This gives us confidence that the solution at four levels of refinement is sufficient. On the other hand, when we employed larger cells in the crust (~ 0.05 R), diffusion became appreciably larger and led to a noticeably smaller pile-up field. The ability to resolve the resistive processes in the crust at a relatively low computational cost is an advantage MHD codes have over hybrid codes: for example, a cell size of ~ 0.06 of a lunar radius was used in the hybrid simulations of Wang et al. (2011) and Fatemi et al. (2017), and a cell size of ~ 0.17 of an asteroid radius (for the asteroid 16 Psyche) was used in Fatemi et al. (2018). In the MHD simulations presented here, we achieved cells that are 3-15 times smaller.

2.2.2. Wake refinement and reconnection

The grid is refined to level 3 along the x axis on the wake side, between $x = -6.0$ R and $x = -1.1$ R. The refinement counteracts the fact that spherical grid cells become larger with radial distance from the origin. The center of the wake is the region where magnetic reconnection occurs: field lines of opposite polarity are pushed inside by the pressure gradient between the flanks of the wake and the void behind the body. It is important to resolve this region to avoid overestimating the rate of reconnection, which is a diffusive phenomenon. Although reconnection is not described by the ideal MHD description, the code mimics its effects by numerical diffusion. Compared to hybrid and particle-in-cell approaches, MHD underestimates the reconnection rate and therefore the rate at which magnetic flux is removed and converted into thermal energy (Birn et al., 2001). Thus, we conclude that MHD will, if anything, destroy less flux and overestimate the remaining magnetic energy in the wake side of the body. We also refer the reader to Section S1 of the Supplemental Material for a comparison of MHD and hybrid

simulations for a body of a similar size showing the large scale structure of the wake is similar.

3. Statistical analysis of present-day IMF variability

An example of the high temporal variability of the solar wind magnetic field can be seen in Fig. S3, representing one day of magnetic field measurements taken close to Earth's orbit in 2007. The data are taken form the OMNI database, a cross-spacecraft calibrated dataset of in-situ solar wind measurements at 1 AU (King & Papitashvili, 2006), available through NASA's CDAWeb (https://cdaweb.sci.gsfc.nasa.gov). The dataset used here is made of 5-minute averages. The magnetic field is measured in a Cartesian reference frame centered on the Earth, where the x axis points toward the Sun, the z axis is normal to the ecliptic plane in the north direction, and the y axis completes a right-handed system.

Fig. S4 shows a statistical analysis of the 1 AU data. In each panel, we plot a histogram of hourly averages of each of the magnetic field components. Each histogram covers a different time interval: a day, a week, a solar rotation, and a year. A similar histogram containing over 22 years of data (equivalent to a full solar cycle) is shown in Fig. 8 in the main text. Over one day, the distributions of the x and y components are centered on a few nT. As the time interval included in the histogram is increased, the distribution becomes more symmetric and the mean value becomes closer to zero, for each of the components (see insets in each panel). These results show that even though the instantaneous magnitude of the IMF is often a few nT, the mean of each component over a year is 10-20 times smaller, and a 100 times smaller when averaged over a solar cycle (see Fig. 8 in the main text). This behavior, which is a direct result of the constant changes in the IMF direction when measured in the ecliptic plane, is critical for assessing the effectivity of the IMF as a source of magnetization.

Another important factor is the angle between the IMF and the solar wind flow direction. The distribution of this angle, using the same data as in panel D of Fig. S4, is shown in Fig. S5. The plot shows the distribution of the angle in a longitude-latitude grid defined over a unit sphere around the measurement point. The data are binned into elements of $0.1° \times 0.1°$ in longitude and latitude, and divided by the total number of points, such that the color contours represent the frequency at which each IMF orientation occurred. We see two clusters, each forming an almost circular distribution

9
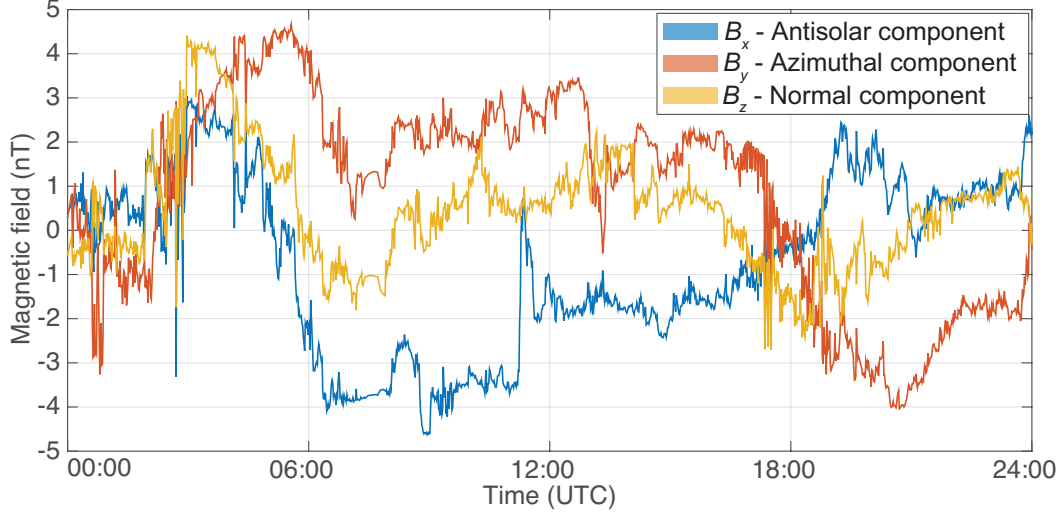
Fig. S3. IMF vector components, B_x, B_y, and B_z, during a representative day in 2007 (during solar minimum), measured in the solar wind at 1 AU. The blue, orange and yellow curves show the x, y, and z components, respectively. These directions are explained in the text. The data are taken from the OMNI database, a cross-spacecraft calibrated dataset of in-situ solar wind measurements at 1 AU (King & Papitashvili, 2006).

with a considerable spread: the standard deviation from the mean direction is $\sim 25°$ in the azimuthal direction and $\sim 30°$ in the polar direction. Each cluster is centered on an azimuthal angle of $45°$ and $135°$, representing the direction of the Parker spiral at 1 AU, but with opposite IMF polarities (for solar wind field lines below and above the heliospheric current sheet). There are relatively few observations where the IMF is actually making a $90°$ angle with the flow. However, the data in Fig. S5 are taken at 1 AU, and the Parker spiral is expected to wind more by 2.5 AU, with the IMF pointing $70°$ away from the flow in the azimuthal direction. The azimuthal component will be even larger for a younger, and faster rotating Sun, suggesting the mean Parker direction would by itself be close to perpendicular to the flow. Nevertheless, the spread around the spiral direction and the flipping of the field across the current sheet is still expected to occur as they are a result of turbulence, shocks, solar rotation, and the solar cycle. All these would be present for a younger, more active, and faster-rotating Sun.
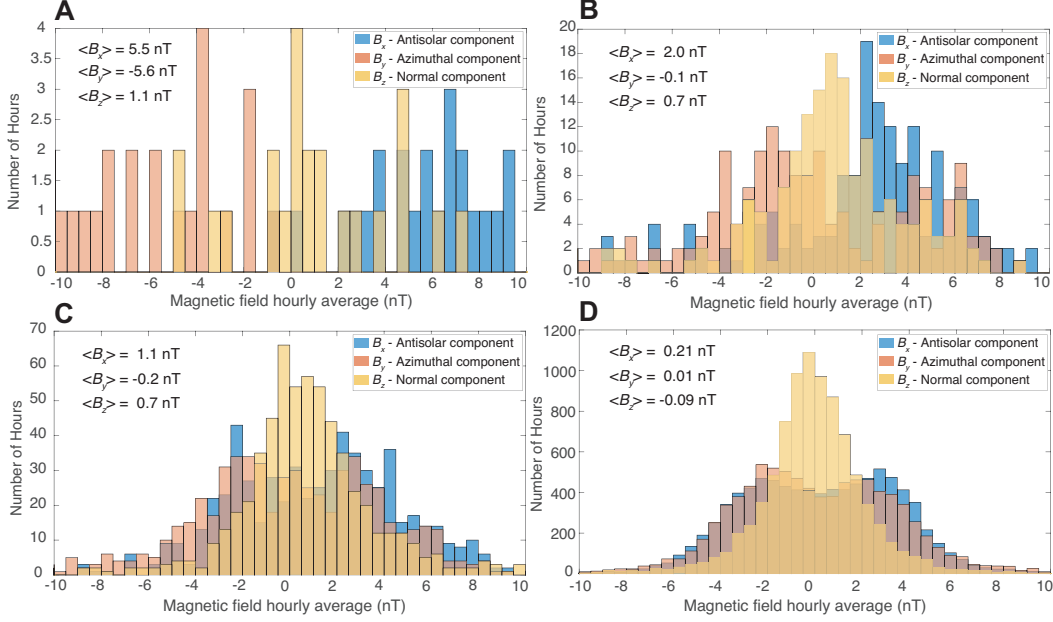
Fig. S4. Histograms of hourly averages of IMF vector components, B_x, B_y, and B_z, measured in the solar wind at 1 AU. Each panel represents the same analysis over a different period: (A) shows data gathered over a day, (B) represents a week, (C) a month, and (D) a year. The color code is the same as in Fig. S3. The data are taken from the 22-year solar wind data, where each period starts in February 1995.

4. Uncertainties in constraining the Parker wind model from observable stellar properties

Equation (1) in the main text describes the variation of the solar wind magnetic field in space, for a given heliocentric distance, r, and polar angle, θ. This formula gives a simple analytical prediction of the large-scale spiral structure of the IMF (which can be seen in the MHD simulation in Fig. 7 in the main text), and the IMF magnitude as a function of location. However, this prediction requires knowledge of the free parameters of equation (1), namely, u_{sw}, R_s, and B_s, which stand for the terminal wind speed, the distance of the source surface, and the magnitude of the field at the source surface, respectively. As mentioned in the main text, these quantities are not well known for the young Sun and for other stars. Any attempt to determine these parameters from the basic stellar properties should take into account the following uncertainties and interdependencies:

- The terminal wind speed, u_{sw}, cannot be constrained directly from observations of other stars. Mass loss rates from young stellar atmo-

11
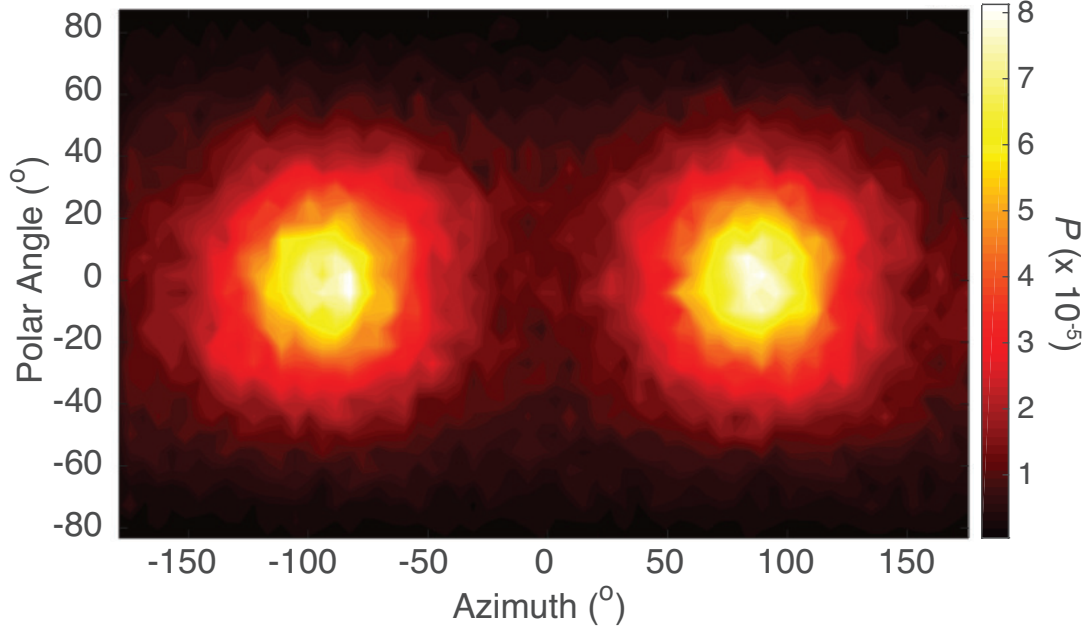
Fig. S5. Distribution of IMF directions, as measured in situ in the solar wind at 1 AU. Data are the same as those used in Fig. S4. IMF directions were calculated with respect to the coordinate system defined in Fig. S3. Azimuth (horizontal axis) is measured in the ecliptic (x-y) plane, where an angle of 0 corresponds to an IMF vector parallel to the x axis. The polar angle (vertical axis) is measured from the ecliptic plane toward the positive z axis (north). The color contours represent the relative probability, P, of each direction.

spheres can be measured (c.f., Wood et al., 2015), but deriving the speed alone is not trivial. In addition, the total mass loss rate decreases non-linearly with increasing rotation rate (Cranmer & Saar, 2011; Cohen et al., 2014), while the distribution of wind speeds around a given star becomes wider with faster rotation (Réville et al., 2016).

- The source surface height, R_s, is defined as the height at which the IMF becomes purely radial. Although a value of 2.5 R_* is commonly used for modeling the present-day solar wind, it can take values between $\sim$2 R_* to $\sim$20 R_* for different magnetic configurations, with the height generally increasing with higher overall dynamo field (Riley et al., 2006; Lee et al., 2011; Réville et al., 2015).

- The field at the source surface, B_s, is naturally related to the strength of the dynamo field, but also to the amount of open flux leaving the Sun. Open field regions make up only 5-20% of the solar surface for the

12

present-day Sun (Wang & Sheely, 1992), and they are expected to be smaller when the magnetic field at the surface becomes stronger (Bravo & Stewart, 1994; Wood et al., 2002).

- Faster rotation (higher Ω_*) increases the azimuthal component of the IMF, as can be seen from equation (1). On the other hand, a faster rotator may produce a faster wind (higher u_{sw}) due to magnetocentrifugal acceleration (Réville et al., 2015). The wind speed, also included in equation (1), would limit the amount by which the azimuthal component can grow due to rotation.

The above arguments justify the need for MHD modeling of a young solar-like star, presented in the main text, since the MHD equations describe both the plasma motion and the magnetic field evolution self-consistently, and can combine the effects of rotation, acceleration, and increased surface fields in a single framework.

5. Determining the solar wind conditions at 2.5 AU for the Sun at 10 My

We used the simulations by Cohen et al. (2010) of the corona of AB Dor as a proxy of the Sun at 10 My (Section 3 in the main text). These simulations allow us to derive the solar wind parameters to be used as input to the present simulations, namely, of the interaction of the young solar wind with the chondritic parent body (Section 6 of the main text). The key steps are choosing which of the AB Dor models in Cohen et al. (2010) is most consistent with the Sun at 10 My and extrapolating the conditions at 2.5 AU from the AB Dor simulations, which extend only up to heliocentric distances of 45 $R_* \sim$0.2 AU. For simplicity, we extrapolate the solar wind properties to 2.5 AU assuming AB Dor's radius is equal to that of the present-day Sun, although it is slightly smaller. We summarize the range of values each parameter may take and the expected impact on the simulation results in Table S4.

5.1. Choice of AB Dor model

Cohen et al. (2010) performed three different simulations of AB Dor's wind, labeled therein as Cases A, B, and C, which differ in the density at the inner boundary of the simulation domain (the coronal base). While stellar parameters such as the magnetic field at the surface and the rotation period

13

are well constrained quantities for wTTS at the age of interest, choosing the appropriate density boundary condition is a more subtle issue. Here we explain which of the cases in Cohen et al. (2010) is most suitable for simulating the young Sun at 10 My.

The amount of mass available to a stellar wind is determined by the density at the base of their coronae (i.e., the plasma that has sufficient thermal energy to expand and overcome the star's gravity). This base density is not an independent property of a star but rather is dynamically determined by processes that elevate material from the photosphere and chromosphere to form the hot and tenuous corona [known as chromospheric evaporation (Klimchuk, 2006)]. These processes are controlled by the coronal heating rate, magnetic topology, and rotation period. MHD models such as those of Cohen et al. (2010) do not aim to simulate these processes and instead set the inner boundary already in the corona, where the plasma has reached 1-5 MK, is fully ionized, and the ideal MHD regime is valid.

Observational estimates of coronal densities, often derived from X-ray images, can give values as high as 1×10^{10} to 1×10^{12} cm^{-3}. As discussed in Cohen et al. (2010), coronal X-ray emission is dominated by the plasma in closed magnetic loops and active regions, while open field regions appear dark at these wavelengths. Since the open regions are those that supply the steady-state wind, they argued that using the observed X-ray density to determine the density at the coronal base of wind models would lead to unrealistic results. This motivated them to explore a range of lower base densities in their modeling. Cases A, B, and C therein applied base densities of 2×10^8, 1×10^9, and 1×10^{10} cm^{-3}, respectively. They found that Case A, when applied to the present-day Sun, led to simulation results that were closest to the observed properties of the present-day wind. Case A is then a good candidate to be used as input to modeling the interaction of the young Sun with the CV parent body.

To further justify the choice of MHD model, we compare the mass loss rates (MLRs) predicted for Cases A, B, and C to available observations of young stars. We focus on this quantity as it is the most relevant quantity for the chondrite magnetization hypothesis for two reasons. First, the MLR reflects the wind speed and density and thus the ram pressure incident on the body. Second, the wind speed determines how much of the star's surface magnetic flux would be transported into interplanetary space. The magnitudes of the modeled MLRs are ordered as Case A < Case B < Case C (with numerical values of 4.5×10^{-13}, 2.1×10^{-12}, and 1.1×10^{-11} $M_\odot$ y^{-1}, respec-

tively; see their Table 2). For comparison, the MLR of the present-day solar wind is 20x smaller than that of Case A.

We compare the above modeled MLRs to observations of 47 stars compiled by Cranmer & Saar (2011). These stars also all have well-constrained properties such as luminosity, rotation period, and magnetic field. Cranmer & Saar (2011) presented a theoretical model relating the MLR to other stellar properties with very good agreement with the data. Most importantly to our purposes, they were able to predict the MLR as a function of time for a 1 $M_\odot$ star, shown in their Fig. 14. Their predictions are consistent with the MLRs predicted by Wood et al. (2015) for the Sun for ages >700 My. The advantage of the Cranmer & Saar (2011) MLR curve is that it extends to much younger ages than those included in Wood et al. (2015). It can be seen that the loss rate decreases as the star leaves the CTTS stage, and reaches a minimum ($\sim 1 \times 10^{-13}$ $M_\odot$ y^{-1}) around the age of 10 My. In comparison, the three MHD simulations of AB Dor all achieve a MLR that is higher than this value. Case A is within the same order of magnitude, while Cases B and C show a significant discrepancy, with MLRs much higher than the Cranmer & Saar (2011) results. This supports the conclusion of Cohen et al. (2010) that the base density of open flux tubes must be significantly smaller than loop densities; only the simulation with the lowest base density tested (Case A) predicted a MLR that is consistent with observed values. The breadth and accuracy of the Cranmer & Saar (2011) observational catalog, together with the thorough examination of the boundary conditions of the MHD model by Cohen et al. (2010) lead us to conclude that Case A is the most realistic MHD wind model for a 10 My Sun that we have available.

Finally, we note that we can make the results even more robust by considering what effects the MLR has on the chondrite magnetization hypothesis. In an MHD stellar model, the wind's velocity, which is almost purely radial, has two opposite effects on the IMF. On one hand, the faster the flow, the larger the open magnetic field regions on the stellar surface (due to stronger stretching of field lines), and thus potentially the larger the IMF. On the other hand, a faster radial flow would lead to a smaller azimuthal component of the IMF, meaning the IMF magnitude would drop faster with radial distance (see equation 1 in the main text). To address these competing effects in the most conservative way, we systematically took upper limits when deriving the IMF at 2.5 AU. We used Case A, which gives the fastest wind model (see Fig. 3 in Cohen et al., 2010), thus taking the maximum of magnetic open flux, but still assumed the field strength drops as $1/r$, as if the field

was purely azimuthal (see Section 3.5 in the main text). The obtained value of 90 nT extrapolated to 2.5 AU was further increased by ∼10% to 100 nT. We conclude that the IMF used as input to the parent body simulations is indeed the maximal possible magnetic field carried by the wind of a 10 My Sun.

5.2. Density at 2.5 AU

The density of the wind at a heliocentric distance r can be found from conservation of the total mass flux through spherical shells:

$$n(r)r^2 = \text{constant}, \tag{1}$$

where n is the number density. This relation is valid for large distances where the radial wind speed has already reached its asymptotic value. The density in the x-z plane of the AB Dor simulation appears in Fig. S6. The density at the edge of the domain varies with latitude. From an examination of the magnetic field in the same plane (Fig. 3 panel D in the main text), we see the higher density regions overlap the location of the heliospheric current sheet (where the magnetic field approaches zero and reverses polarity). We are interested in the main component of the solar wind away from the current sheer, and thus place an upper limit of 5,000 cm^{-3} for the density at 45 R_*. Using the above formula, this gives $n(2.5 \text{ AU}) < 35$ cm^{-3}.

5.3. Temperature at 2.5 AU

The temperature around AB Dor in the x-z plane is shown in Fig. S7. The typical temperature at 45 R_* does not exceed 500,000 K. We can derive the temperature at 2.5 AU using two limiting approximations:

- The solar wind is isothermal due to its high thermal conductivity.

- The wind is cooling off with distance due to its expansion.

The first approximation simply means the wind retains the same temperature. In reality, the temperature depends on high order effects such as non-isotropic heat conduction, shocks, and turbulent heating, but it is safe to assume that over large scales the temperature will not increase with distance. Thus, the isothermal case gives an upper limit for the wind temperature at 2.5 AU, namely 500,000 K (see Table S4). This is consistent with Parker

(1958), which showed that as long as there are no heat sources far from the Sun, the temperature would decrease with distance as:

$$T(r) = T_0 \left(\frac{r_0}{r}\right)^a.$$ (2)

This brings us to the second approximation of a cooling wind. If adiabatic expansion is assumed, $a = 4/3$, giving a temperature of 18,000 K at 2.5 AU. However, it is known that the solar wind does not cool adiabatically (Scudder et al., 2015), so the parameter a should be smaller to produce a more realistic decrease with distance. As input for the simulations, we choose a lower limit of the temperature at 2.5 AU to be 50,000 K. For comparison, typical solar wind values at 1 AU for the present-day wind are around 100,000-200,000 K.
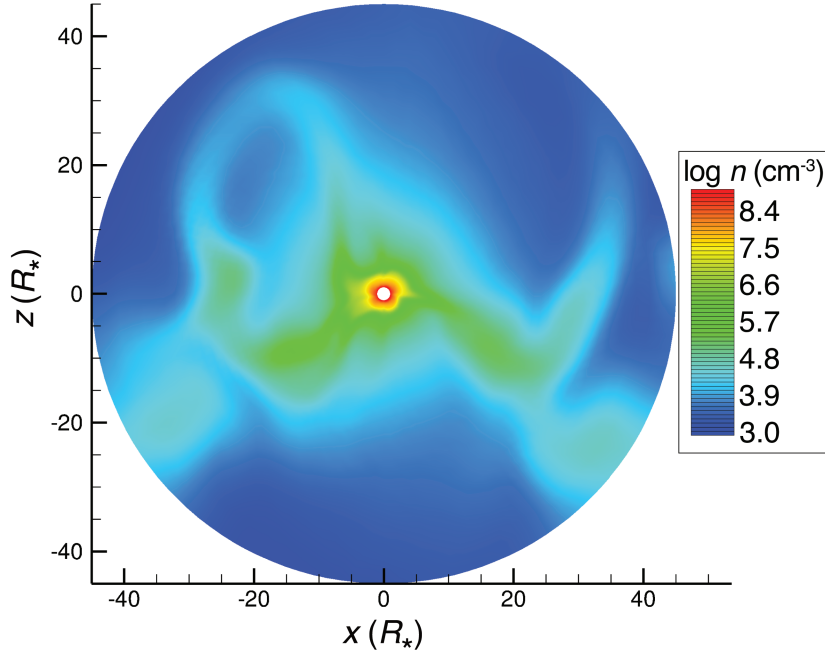
Fig. S6. Log of the particle density in the x-z plane around the star AB Dor. Data taken from the simulations in Cohen et al. (2010) and described in Section 3 in the main text.

5.4. Wind speed at 2.5 AU

Fig. 3 in the main text shows that the radial speed of the solar wind around AB Dor reached 600-700 km s^{-1} by 45 R_*, especially around the

17
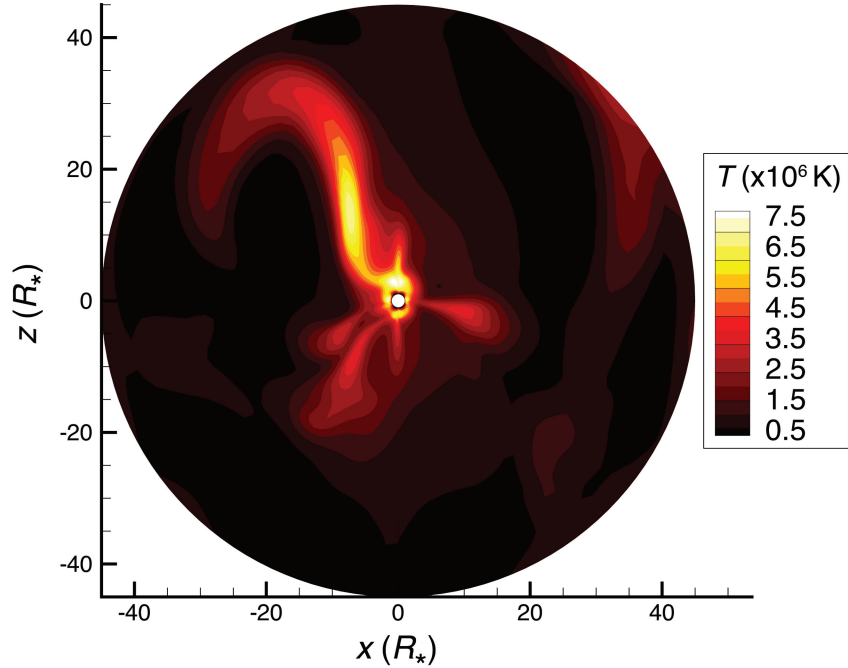
Fig. S7. Plasma temperature in the x-z plane around the star AB Dor. Data taken from the simulations in Cohen et al. (2010) and described in Section 3 in the main text.

ecliptic plane. Although this is the most probable speed, there are some faster streams which have speeds up to 1,100 km s^{-1}. The fastest wind streams are only a small part of the wind. Although the fastest streams do not reach the ecliptic plane, with changes in the magnetic configuration expected during the solar cycle fast streams may well reside in the ecliptic plane. To cover all cases, we will use both speeds as input to different simulations (Table S4). We note that the density of the solar wind would also vary between fast and slow streams. In fact, the momentum flux at 1 AU is distributed almost evenly, with the difference between fast and slow stream being $\sim 8\%$ (Schwenn, 1990). Thus, if we take the momentum flux as $nu_{sw}^2 = \text{constant}$, where n is the solar wind density, we find that when the speed is 1,100 km $^{-1}$, the density would be adjusted to 14 cm^{-3}. This is summarized in Table S4.

18

Supplementary Tables

Table S1. Paleomagnetic measurements of post-accretional magnetization in chondrites.

Meteorite	Group and Type	$P.I.$ (μT)	Age (My)	Method	Reference
Allende	CV3	$\sim 60.0^{*}$	$9 - 10$	Thellier-Thellier, ARM, and IRM	Carporzen et al. (2011)
Kaba MC/MT	CV3	$1.6 - 6.0^{**}$	$> 6 - 10$	Thellier-Thellier	Gattacceca et al. (2016)
Mighei	CM2	> 1.0	$> 2.4 - 4$	IRM	Cournède et al. (2015)
Murchison	CM2	> 1.0	$> 2.4 - 4$	IRM	Cournède et al. (2015)
Murray	CM2	> 2.0	$> 2.4 - 4$	IRM	Cournède et al. (2015)
Nogoya	CM2	> 1.0	$> 2.4 - 4$	IRM	Cournède et al. (2015)
Cold Bokkeveld	CM2	$> 0.6^{\dagger}$	$> 2.4 - 4$	IRM	Cournède et al. (2015)
Paris	CM2	$> 2.0^{\dagger\dagger}$	$> 2.4 - 4$	IRM	Cournède et al. (2015)
Portales Valley	H6	1.0-40.0	100	XPEEM	Bryson et al. (2016)

Note: The first column lists the meteorite name, the second column lists the chondrite group and petrologic type, the third column lists the mean paleointensity (or mean estimate of a lower limit on the paleointensity), $P.I.$, typically estimated from several subsamples, the fourth column lists the inferred NRM acquisition time in My after CAI formation, the fifth column lists the paleointensity method [Thellier-Thellier (see chapter 10 in Tauxe, 2010), isothermal remanent magnetization (IRM; see Gattacceca & Rochette, 2004; Tikoo et al., 2014), anhysteretic remanent magnetization (ARM; see Tikoo et al., 2014), or X-ray photoemission electron microscopy (XPEEM; see Bryson et al., 2014)], and the sixth column lists the reference for the study. The paleointensity for Allende is that of the MT component, taken from the alteration-corrected Thellier-Thellier experiments described in the Supplemental material of Carporzen et al. (2011). The Kaba paleointensity is the average of the medium coercivity/medium temperature (MC/MT) component in 5 samples as reported in Table 2 of Gattacceca et al. (2016). This study established post-accretional magnetization but did not check for unidirectionality. The CM2 chondrite data are for samples inferred to have preterrestrial HC components (see Table 3 and Section 5.2 in Cournède et al. (2015).
* The minimum inferred paleointensity is $\sim 20~\mu$T.
** Calculated from the thermal and two AF-based paleointensity measurements and corrected for the fraction of unmagnetized chondrules (see final paragraph of Section 4.3 of Gattacceca et al., 2016).
† Calculated from Section 5.2 in Cournède et al. (2015) that states that the mean lower limit measured in Cold Bokkeveld samples was $2.1 \pm 1.5~\mu T$. The absolute lower limit is then taken to be $2.1 - 1.5 = 0.6~\mu T$.
†† Determined from the measured HC components of six mutually oriented samples of the Paris meteorite listed in Table 3 of Cournède et al. (2015)

Table S2. Paleomagnetic measurements of pre-accretional magnetization in chondrites.

Meteorite	Group	*P.I.* (μT)	Age (My)	Method	Reference
Semarkona	LL3 chondrite	$5 - 54$	$1 - 3$	IRM and ARM	Fu et al. (2014)
D'Orbigny, Sahara 99555, and Asuka 881371	angrites	< 0.6	3.8	IRM and ARM	Wang et al. (2017)
Kaba	CV3 chondrite	< 0.3	$4 - 6$	Thellier-Thellier	Gattacceca et al. (2016)
NWA 7325	ungrouped achondrite	< 1.6	4.2	IRM, ARM, and thermal	Weiss et al. (2017)

Note: The first column lists the meteorite names, the second column lists the meteorite group, the third column lists the paleointensity, *P.I.*, the fourth columns lists the age of the paleointensity constraint, the fifth column lists the paleointensity method [Thellier-Thellier; see chapter 10 in Tauxe et al. 2010), isothermal remanent magnetization Gattacceca & Rochette (IRM; see 2004); Tikoo et al. (IRM; see 2014), anhysteretic remanent magnetization (ARM; see Tikoo et al., 2014)], and the sixth column lists the reference. The paleointensity age is measured in My after CAI formation.

Table S3. Observed and modeled stellar properties

Object	Radius ($R_\odot$)	Mass ($M_\odot$)	Rotation Period (day)	Age (My)	Coronal Temperature (MK)	Mean Surface Field (mT)
Present-day Sun	1	1	26	4500	1-10	0.1-1
Sun at 10 My (wTTS)	>1	1	0.5-1	10	1-10	10-20
AB Doradus	0.86-0.96	0.76-0.86	0.5	30-125	3-30	22
AB Dor model input	0.86	0.76	0.5	–	5	22

Note: The first column lists the stellar object name, the second column lists the stellar radius, the third column lists the stellar mass, the fourth column lists the rotation period, the fifth column lists the approximate age, the sixth column lists the coronal temperature, and the last column lists the mean field at the surface, given by the unsigned flux averaged over the surface. The first row lists the properties of the present day Sun (Gombosi, 1999). The second row lists the estimated properties of the Sun at 10 My derived from observations of wTTS [rotation period from Marilli et al. (2005); Karim et al. (2016); coronal temperatures from Schulz (2012), and magnetic fields from Gregory et al. (2012); Vidotto et al. (2014, 2016); Folsom et al. (2016); Kochukhov et al. (2017)]. The third row lists the observed properties of AB Doradus [radius taken from Maggio et al. (2000) and Guirado et al. (2011), for the lower and upper limit, respectively; mass range taken from Maggio et al. (2000) and Guirado et al. (2006) for the lower and upper limit, respectively; rotation period taken from Pakull (1981); estimated age range taken from Drake et al. (2015); coronal temperature taken from Sanz-Forcada et al. (2003) and García-Alvarez et al. (2005); mean magnetic field calculated from the ZDI map of AB Doradus used in Cohen et al. (2010)]. The last row lists the input parameters for modeling AB Doradus in Cohen et al. (2010). The full ZDI map (rather than the mean magnetic field) is an input to the model and the mean field is calculated here for comparison.

Table S4. Constraint on free parameters and most favorable values.

Parameter	Minimum value	Maximum value	Most likely/ mean value	Most favorable value
Body radius (km)	unknown	470	–	470
Crust thickness (km)	0.01	0.1	–	0.01
Wind speed (km s^{-1})	600	1,100	700	1,100
Temperature (K)	50,000	500,000	–	500,000
Angle between IMF and flow ($^\circ$)	0	180	75	90

Note: The first column lists the input parameters for the MHD simulations of an asteroid with the solar wind. The second and third columns list the minimum and maximum values these parameters may feasibly take. The forth column lists what is the most likely value this parameter may take, while the fifth column lists the value that would be most favorable for field enhancement at the body (and hence, for the magnetization of the parent body by the solar wind). The information in the first two rows pertain to the size and crustal thickness of the CV chondrite parent body, respectively (derived in Section 4 in the main text). Only the upper limit was derived for the parent body size, while the lower limit is not known and in any case a smaller body would produce a smaller field compression. The third and forth rows show the ranges of wind parameters at 2.5 AU extrapolated from the MHD simulation of AB Dor (see Section S5). The fifth row lists the range of values for the angle between the IMF and the wind velocity, based on the IMF statistics at 1 AU. The most favorable value is given by the Parker spiral angle (see Section S2 and Section 7 in the main text).

Supplementary References

Birn, J., Drake, J. F., Shay, M. A., Rogers, B. N., Denton, R. E., Hesse, M., Kuznetsova, M., Ma, Z. W., Bhattacharjee, A., Otto, A., Pritchett, P. L., 2001. Geospace environmental modeling (GEM) magnetic reconnection challenge. J. Geophys. Res. 106, 3715-3719.

Bravo, S., Stewart, G., 1994. Evolution of polar coronal holes and sunspots during cycles 21 and 22. Sol. Phys. 154, 377-384.

Bryson, J. F. J., Herrero-Albillos, J., Kronast, F., Ghidini, M., Redfern, S. A. T., van der Laan, G., Harrison, R. J., 2014. Nanopaleomagnetism of meteoritic Fe-Ni studied using X-ray photoemission electron microscopy. Earth Planet. Sci. Lett. 396, 125-133.

Bryson, J. F. J., Weiss , B. P., Scholl, A., Getzin, B. L., Abrahams , J. N. H., Nimmo, F. , 2016. Paleomagnetic evidence for a partially differentiated H chondrite parent planetesimal. AGU Fall Meeting Abstracts, 2016.

Carporzen, L., Weiss, B.P., Elkins-Tanton, L.T., Shuster, D.L., Ebel, D.S., Gattacceca, J., 2011. Magnetic evidence for a partially differentiated carbonaceous chondrite parent body. Proc. Natl. Acad. Sci. USA 108, 6386-6389.

Cohen, O., Drake, J. J., Kashyap, V. L., Hussain, G. A. J., Gombosi, T. I., 2010. The coronal structure of AB Doradus. Astrophys. J. 721:80-89.

Cohen, O., Drake, J. J., 2014. A grid of MHD models for stellar mass loss and spin-down rates of solar analogs. Astrophys. J. 783-55 (11pp).

Cournède, C., Gattacceca, J., Gounelle, M., Rochette, P., Weiss, B.P., Zanda, B., 2015. An early solar system magnetic field recorded in CM chondrites. Earth Planet. Sci. Lett. 410, 62-74.

Cranmer, S. R., Saar, S. H., 2011. Testing a predictive theoretical model for the mass loss rates of cool stars. Astrophys. J. 741, 54.

Drake, J. J., Chung, S. M., Kashyap, V. L., Garcia-Alvarez, D., 2015. X-Ray evidence for a pole-dominated corona on AB Dor. Astrophys. J. 802, 62.

Fatemi, S., Poppe, A. R., Delory, G. T., Farrell, W. M., 2017. AMITIS: A 3D GPU-based hybrid-PIC model for space and plasma physics, J. of Phys.: ASTRONUM-2016 Conf. Proc. Series, 837, 012017.

Fatemi, S., Poppe, A. R., 2018. Solar Wind Plasma Interaction with Asteroid 16 Psyche: Implication for Formation Theories. Geophys. Res. Lett. 45, 39-48.

Folsom, C. P., Petit, P., Bouvier, J., Lèbre, A., Amard, L., Palacios, A., Morin, J., Donati, J. F., Jeffers, S. V., Marsden, S. C., Vidotto, A. A., 2016. The evolution of surface magnetic fields in young solar-type stars - I. The first 250 Myr. Mon. Not. R. Astron. Soc. 457, 580-607.

Fu, R. R., Weiss, B. P., Lima, E. A., Harrison, R. J., Bai, Xue-Ning, Desch, S. J., Ebel, D. S., Suavet, C., Wang, H., Glenn, D., Le Sage, D., Kasama, T., Walsworth, R. L., Kuan, A. T., 2014. Solar nebula magnetic fields recorded in the Semarkona meteorite. Science 346, 1089-1092.

García-Alvarez, D., Drake, J. J., Lin, L., Kashyap, V. L., Ball, B., 2005. The coronae of AB Doradus and V471 Tauri: Primordial angular momentum versus tidal spin-up, 2005. Astrophys. J. 621, 1009-1022.

Gattacceca, J., Rochette, P., 2004. Toward a robust normalized magnetic paleointensity method applied to meteorites. Earth Planet. Sci. Lett. 227, 377-393.

Gattacceca, J., Weiss, B.P., Gounelle, M., 2016. New constraints on the magnetic history of the CV parent body and the solar nebula from the Kaba meteorite. Earth Planet. Sci. Lett. 455, 166-175.

Gombosi, T. I., 1999. Physics of the Space Environment. ISBN 052159264X, Cambridge University Press.

Gregory, S. G., Donati, J. F., Morin, J., Hussain, G. A. J., Mayne, N. J., Hillenbrand, L. A., Jardine, M., 2012. Can we predict the global magnetic topology of a pre-main-sequence star from its position in the Hertzsprung-Russell diagram? Astrophys. J. 755, 97.

Guirado, J. C., Martí-Vidal, I., Marcaide, J. M., Close, L. M., Algaba, J. C., Brandner, W., Lestrade, J. F., Jauncey, D. L., Jones, D. L., Preston, R.

A., Reynolds, J. E., 2006. On the dynamics of the AB Doradus system. Astron. Astrophys. 446, 733-738.

Guirado, J. C., Marcaide, J. M., Martí-Vidal, I., Le Bouquin, J. B., Close, L. M., Cotton, W. D., Montalbán, J., 2011. The size of AB Doradus A from VLTI/AMBER interferometry. Astron. Astrophys. 533, A106.

Jia, X., Slavin, J. A., Gombosi, T. I., Daldorff, L. K. S., Toth, G. van der Holst, B., 2015. Global MHD simulations of Mercury's magnetosphere with coupled planetary interior: Induction effect of the planetary conducting core on the global interaction. J. Geophys. Res. 120, 4763-4775.

Karim, M. T., Stassun, K. G., Briceo, C., Vivas, A. K., Raetz, S., Mateu, C., Downes, J. J., Calvet, N., Hernndez, J., Neuhuser, R., Mugrauer, M., Takahashi, H., Tachihara, K., Chini, R., Cruz-Dias, G. A., Aarnio, A., James, D. J., Hackstein, M., 2016. The rotation period distributions of 4-10 Myr T Tauri stars in Orion OB1: new constraints on pre-main-sequence angular momentum evolution. Astrophys. J. 152, 198.

Kallio, E., Wurz, P., Killen, R., McKenna-Lawlor, S., Milillo, A., Mura, A., Massetti, S., Orsini, S., Lammer, H., Janhunen, P., Ip, W. H., 2008. On the impact of multiply charged heavy solar wind ions on the surface of Mercury, the Moon and Ceres, Planet. Space Sci., 56, 1506-1516.

[dataset] King, J., Papitashvili, N., 2006. 5 minute averaged definitive multi-spacecraft interplanetary parameters data (OMNI_HRO_5MIN), available on NASA CDAWeb: https://cdaweb.sci.gsfc.nasa.gov

Kochukhov, O., Petit, P., Strassmeier, K. G., Carroll, T. A., Fares, R., Folsom, C. P., Jeffers, S. V., Korhonen, H., Monnier, J. D., Morin, J., Rosén, L., Roettenbacher, R. M., Shulyak, D., 2017. Surface magnetism of cool stars. Astron. Nachr. 338, 428-441.

Klimchuk, J. A., 2006. On solving the coronal heating problem. Solar Phys. 234, 2, 41-77.

Lee, C. O., Luhmann, J. G., Hoeksema, J. T., Sun, X., Arge, C. N., de Peter, I., 2011. Coronal field opens at lower height during the solar cycles 22 and 23 minimum periods: IMF comparison suggests the source surface should be lowered. Solar Phys. 269: 367-388.

Maggio, A., Pallavicini, R., Reale, F., Tagliaferri, G., 2000. Twin X-ray flares and the active corona of AB Dor observed with BeppoSAX. 356, 627-642.

Marilli, E., Frasca, A. Alcalá, J. M., Catalano, S., Covino, E., 2005. Rotational periods of solar-mass WTTS in Orion. Mem. S.A.It. Vol. 76, 358.

Omidi, N., Blanco-Cano, X., Russel, C. T., Karimabadi, H., and Acuna, M., 2002. Hybrid simulations of solar wind interaction with magnetized asteroids: General characteristics. J. Comput. Phys. 107, A12, 1487.

Oran, R., Weiss, B. P., 2017. Were chondrite parent bodies magnetized by the early solar wind? In: Proc. Lunar Planet. Sci. Conf., vol. 48, pp. 2958.

Pakull, M. W., 1981. HD 36705 - A new bright X-ray emitting RS CVn star. Astron. Astrophys. 104, 33-36.

Parker, E. N., 1958. Dynamics of the interplanetary gas and magnetic field. Astrophys. J. 128, 664.

Réville, V., Brun, A. S., Strugarek, A., Matt, S. P., Bouvier, J., Folsom, C. P., Petit, P., 2015. From solar to stellar corona: The role of wind, rotation, and magnetism. Astrophys. J. 814, 99.

Réville, V., Folsom, C. P., Strugarek, A., Brun, A. S., 2016. Age dependence of wind properties for solar type stars: A 3D study. Astrophys. J. 832, 145.

Riley, P., Linker, J. A., Mikić, Z., Lionello, R., Ledvina, S. A., Luhmann, J. G., 2006. A comparison between global solar magnetohydrodynamic and potential field source surface model results. Astrophys. J. 653, 1510-1516.

Sanz-Forcada, J., Maggio, A., Micela, G., 2003. Three years in the coronal life of AB Dor. I. Plasma emission measure distributions and abundances at different activity levels. Astron. Astrophys. 408, 1087-1102.

Scudder, J. D., 2015. Radial variation of the solar wind proton temperature: Heat flow or addition? Astrophys. J. 809:126.

Schulz, N. S., 2012. The formation and early evolution of stars: from dust to stars and planets, In: Astronomy and Astrophysics Library, Springer-Verlag Berlin Heidelberg.

Schwenn, R., 1990. Large-scale structure of the interplanetary medium. In: Physics and Chemistry in Space - Space and Solar Physics, Vol. 20. Physics of the Inner Heliosphere I, Editors: Schwenn, R. & Marsch, E., pp 99. Springer-Verlag Berling Heidelberg 1990.

Simon, S., Bagdonat, T., Motschmann, U., Glassmeier, K. H., 2006. Plasma environment of magnetized asteroids: a 3-D hybrid simulation study. Ann. Geophys. 24, 407-414.

Tauxe, L., 2010. Essentials of paleomagnetism, xvi, 489 p., University of California Press, Berkley.

Tikoo, S. M., Weiss, B. P., Cassata, W. S., Shuster, D. L., Gattacceca, J., Lima, E. A., Suavet, C., Nimmo, F., Fuller, M. D., 2014. Decline of the lunar core dynamo. Earth Planet. Sci. Lett. 404, 89-97.

Tóth, G., van der Holst, B., Sokolov, I. V., De Zeeuw, D. L., Gombosi, T. I., Fang, F., Manchester, W. B., Meng, X., Najib, D., Powell, K. G., Stout, Q. F., Glocer, A., Ma, Y., Opher, M., 2012. Adaptive numerical algorithms in space weather modeling. J. Comput. Phys. 231, 3, 870-903.

Vidotto, A. A., Gregory, S. G., Jardine, M., Donati, J. F., Petit, P., Morin, J., Folsom, C. P., Bouvier, J., Cameron, A. C., Hussain, G., Marsden, S., Waite, I. A., Fares, R., Jeffers, S., do Nascimento, J. D., 2014. Stellar magnetism: empirical trends with age and rotation. Mon. Not. R. Astron. Soc. 441, 2361-2374.

Vidotto, A. A., 2016. Stellar magnetism, winds and their effects on planetary environments, In: 19th Cambridge Workshop on Cool Stars, Stellar Systems, and the Sun (CS19), 147.

Wang, H., Weiss, B. P., Bai, X. N., Downey, B.G., Wang, J., Wang, J., Suavet, C., Fu, R. R., Zucolotto, M. E., 2017. Lifetime of the solar nebula constrained by meteorite 121 paleomagnetism. Science 355, 623-627.

Wang, Y. C., Müller, J., Ip, W. H., Motschmann, U., 2011. A 3d hybrid simulation study of the electromagnetic field distributions in the lunar wake. Icarus 216, 415-425.

Wang, Y. M., Sheely, Jr., N., R., 1992. On potential field models of the solar corona. Astrophys. J. 392, 310-319.

Weiss, B. P., Wang, H., Sharp, T. G., Gattacceca, J., Shuster, D. L., Downey, B., Hu, J., Fu, R. R., Kuan, A. T., Suavet, C., Irving, A. J., Wang, J., Wang, J., 2017. A nonmagnetic differentiated early planetary body. Earth Planet. Sci. Lett. 468, 119-132.

Wood, B. E., Müller, H., Zank, G. P., Linsky, J. L., 2002. Measured mass-loss rates of solar-like stars as a function of age and activity. Astrophys. J. 574, 412-425.

Wood, B.E., Linsky, J.L., Gudel, M., 2015. Stellar winds in time. In: Lammer, H., Khodachenko, M. (Eds.), Characterizing stellar and exoplanetary environments. In: Astrophysics and Space Science Library, vol. 41, pp. 19-35.